

Polarized Target Nuclear Magnetic Resonance Measurements with Deep Neural Networks

D. Seay · I. P. Fernando · D. Keller

Received: date / Accepted: date

Abstract Continuous-wave Nuclear Magnetic Resonance (CW-NMR) operated in constant-current mode has served as a foundational technique for polarization measurement in solid-state dynamically polarized targets within nuclear and high-energy physics experiments for several decades, and it remains an essential tool. Conventional Q-meter-based phase-sensitive detection is critical for precise real-time determination of target polarization during scattering runs. However, the accuracy and reliability of these measurements are frequently compromised by elevated noise levels, baseline drift, and systematic uncertainties arising from signal isolation and fitting, ultimately degrading the overall experimental figure of merit. In this work, we report the first successful application of neural network architectures to continuous-wave NMR polarization metrology. By leveraging advanced machine learning techniques for signal extraction and denoising, we achieve a substantial reduction of fitting uncertainties under a variety of realistic simulated and experimental conditions. These improvements translate directly into more robust real-time (online) polarization monitoring and significantly higher precision in subsequent offline analysis. The resulting methodology offers an improved figure of merit for scattering experiments employing dynamically polarized targets and establishes a new tools for NMR-based polarimetry in high-energy and nuclear physics.

Keywords Q-meter, Nuclear Magnetic Resonance (NMR), Dynamic Nuclear Polarization (DNP), Polarized Targets, Solid-State Targets, Machine Learning (ML),

This work was supported by the Department of Energy (DOE), United States of America contract DE-FG02-96ER40950.

Department of Physics, University of Virginia, Charlottesville, Virginia 22904, USA

Artificial Neural Networks (ANN), Deep Neural Networks (DNN)

1 Introduction

Continuous-wave Nuclear Magnetic Resonance (CW-NMR) remains the method of choice for real-time polarization monitoring in solid-state dynamically polarized targets employed in nuclear and high-energy physics scattering experiments. The standard implementation relies on resonant Q-meters operated in constant-current mode, which facilitate phase-sensitive detection of the absorptive and dispersive components of the RF susceptibility[6]. Although this approach is mature and widely fielded, its performance under realistic experimental conditions is often fundamentally constrained by multiple degradation mechanisms: baseline distortions, abrupt detuning caused by cable discontinuities or mechanical perturbations of the resonant circuits, radio-frequency (RF) interference inherent to experimental environments, and limitations on clean power. Consequently, conventional polarization extraction techniques—whether based on thermal-equilibrium (TE) calibration scaling or analytic lineshape fitting—typically incur relative uncertainties of several percent arising solely from fitting systematics. At low polarization levels, as well as in weak NMR signals in general, where the NMR signal amplitude becomes comparable to the prevailing noise floor, stochastic fluctuations and measurement-to-measurement variability further degrade both accuracy and precision. Even under optimal conditions, the widely used Liverpool Q-meter (described in Sec. 2) exhibits an intrinsic relative uncertainty of approximately 1% relative. The increasing demand for accurate polarization measurements across a broad

spectrum of facilities, from high-luminosity hadron and lepton beamlines to various meson and photon beam experiments, underscores the need for measurement methods that remain robust against baseline skew, tune drift, elevated noise, and deliberate RF field modulation. Modern machine learning techniques, particularly deep artificial neural networks (ANNs), are ideally suited to address some of these challenges. By training on large, physically accurate ensembles of simulated CW-NMR signals that systematically incorporate variations in circuit parameters, environmental noise, baseline morphology, and target-specific lineshapes, neural networks can learn highly nonlinear mappings from raw complex voltage and phase to polarization with full uncertainty quantification. This approach eliminates the need for real-time analytic fitting during online monitoring, enhances resilience to RF artifacts, and preserves or improves ultimate accuracy and precision for both spin-1/2 and spin-1 systems.

In this work, we report the first comprehensive application of deep neural networks to polarization metrology using Q-meter-based CW-NMR. For spin-1/2 targets, we introduce a novel area-integration methodology that yields stable and unbiased polarization estimates even in the presence of severe baseline shifts and noise contamination. For spin-1 systems exhibiting a Pake doublet (characteristic of deuterated targets in non-cubic lattices), we simultaneously extract vector and tensor polarizations using two complementary neural-network paradigms: an enhanced area-based technique and a direct lineshape-regression. We present detailed performance benchmarks, compare the robustness and uncertainty budgets of the respective methods, validate against conventional analyses on experimental data, and discuss pathways toward real-time deployment and further refinement.

The remainder of this paper is organized as follows: Section 2 covers the fundamentals of the Liverpool Q-meter. Section 3 reviews the relevant spin-1 NMR theory, including the analytical deuteron lineshape and its relation to vector and tensor polarization. Section 4 describes the Liverpool Q-meter system, the full RF circuit model, and the simulation framework used to generate realistic training data, including sources of baseline distortion and noise. Section 5 presents the architecture, training strategy, and performance of the artificial neural networks developed for polarization and signal area extraction as well as discussions on the use of denoising autoencoders (DAEs). Section 6 summarizes the results, compares the ANN predictions with traditional TE and lineshape fitting methods, and discusses the implications for real-time polarimetry. Section 7 suggests how these tools can be used to extract tensor polarization enhanced

target. Finally, Section 8 summarizes the paper and outlines future plans.

2 Liverpool Q-meter System

Polarization measurements of the target sample are performed using a system equipped with a Liverpool Q-meter [6]. The Q-meter operates in conjunction with a data-acquisition system to record the voltage at each frequency step within its operational range of 3–300 MHz, enabling measurements of materials whose Larmor frequencies fall within this bandwidth.

The target signal is carried through a special copper coaxial transmission line whose total electrical length is constructed to be an integer multiple of $\lambda/2$, where λ is the wavelength corresponding to the Larmor frequency of the target material in the cable (i.e., scaled by the cable's velocity factor). Because a transmission line reproduces its input impedance every $\lambda/2$, using an integer number of half-wavelength sections ensures that the phase of the detected NMR signal is preserved and that the resonant lineshape at the Q-meter remains undistorted at a single frequency. Sweeping across a center frequency, however, slightly decouples the outgoing-incoming signal phase due to influences from reactive components. For typical coaxial cables with a velocity factor of approximately 0.78 (for cables with a foam/PTFE dielectric), the electrical half-wavelength is approximately 55 cm at 213 MHz (the proton Larmor frequency at 5 T) and approximately 360 cm at 32.7 MHz (The central deuteron Larmor frequency at 5 T). Accurate knowledge of this electrical length is essential: even modest deviations from an exact $n\lambda/2$ configuration introduce shifts in the circuit's Q-curve that appear as left- or right-leaning asymmetries in the continuous-wave NMR baseline.

In the Liverpool Q-meter [6] and its descendants—the current through the target coil is held constant while the complex voltage developed across the low-impedance tuned circuit is measured. A RF phase-sensitive detector, referenced to the coil current itself, extracts the *real part* of this voltage (V_R). This real-part signal is directly proportional to the total effective series resistance of the resonant circuit. The absorptive component of the nuclear susceptibility $\chi''(\omega)$ (whether from energy-absorbing or energy-emitting spin transitions) therefore manifests as a small positive or negative change in circuit loss, appearing as a proportional variation in V_R that is essentially linear with polarization over a wide dynamic range. By contrast, the dispersive component $\chi'(\omega)$ primarily causes a slight detuning of the resonant frequency; because the measurement is performed with a fixed-frequency sweep rather than by tracking the resonance, χ' does not produce an independent orthogonal dispersion channel but instead

contributes to the characteristic sloping Q-curve background. The Q-meter design configuration prioritizes the real part of the output voltage—rather than magnitude and phase or separate absorption and dispersion quadratures—which significantly improves linearity (nonlinearity typically below 0.2–1%) and strongly suppresses the amplitude of the Q-curve background. The primary polarization signal is carried almost exclusively by the real-part (absorption-dominated) channel, with residual dispersive effects treated as baseline contributions to be removed by careful tuning, cable-length optimization, temperature stabilization, or modern subtraction and modeling techniques. Tuning ensures that the Q-meter operates optimally for a given experimental configuration. The $\lambda/2$ transmission line must be set to the correct electrical length to ensure proper system performance, while a variable capacitor is adjusted to balance the in-parallel inductor-capacitor (LC) tank of the circuit and achieve impedance matching between the Q-meter reference circuit and the inductive coil containing the target sample. In addition, phase tuning is performed to minimize reactive components, thereby isolating the real (in-phase) component of the signal. The imaginary (quadrature) component is separated by a $\pi/2$ phase shift improving the fidelity of phase-sensitive detection. We note here that being out of tune with either the cable-length or the phase frequently leads to errors in the extraction, especially when these changes are due to spontaneous jumps from mechanical shifts during data acquisition. These types of shifts can be corrected using a lineshape theory that accommodates functionality outside of a perfect tune.

Standard polarization measurement techniques employing Q-meter-based NMR systems in scattering experiments typically achieve relative uncertainties at the level of 3–5% [17]. These uncertainties are dominated by limitations in polarization calibration—most notably those associated with thermal equilibrium measurements—and by fitting-related uncertainties. Additional contributions arise from magnetic-field inhomogeneity, temperature drifts in the readout electronics, imperfect knowledge of the coil filling factor, 3D distribution of polarization in the sample, baseline distortions, statistical fluctuations, and limitations in pressure or temperature measurement and calibration. The dominance of these individual error sources is discussed in Sec. 2.2.

Neural networks provide a powerful framework for improving both the accuracy and precision of polarization measurements extracted from continuous-wave NMR signals, primarily through the reduction of fitting-related uncertainties and, to a more limited extent, certain systematic components. By learning highly nonlinear mappings directly from raw detector outputs, these models

can be trained to minimize the full polarization covariance across a wide range of experimental conditions. Moreover, their ability to generalize beyond the training data enables partial mitigation of some instrumental limitations (jumps in baseline and tune shifts) that are difficult to address using traditional analysis techniques.

In the specific context of the Liverpool Q-meter, the observed baseline shape, signal lineshape, and amplitude-to-polarization relationship are all influenced by subtle, interdependent instrumental effects. Traditional analytical calibration is capable of reaching the lower 1% uncertainty bound but only under optimal conditions. A suitably trained neural network, by contrast, can implicitly capture these complex interactions and correct for them, provided it is trained on realistic data that encodes the full range of instrumental characteristics. To achieve this, we require high-quality training data generated from simulations that capture all relevant dependencies and the leading contributions to the full covariance.

To generate such training data, an accurate circuit model of the entire Q-meter system—including the oscillator dynamics, transmission-line behavior, probe tuning characteristics, and known sources of systematic error—was implemented (see Sec. 2.2 for a complete inventory of the modeled effects). By sampling this model over the relevant parameter space, we produced large, physically realistic datasets of the Q-meter circuit behavior (baseline or Q-curve). We then add the signal lineshape with various types of noise and tune characteristics (or off tune variations) and perform Monte Carlo (MC) sampling to produce experimentally realistic baseline and polarization data for high statistics training and testing.

2.1 Circuit Theory

We develop a python based Q-meter circuit simulation based on the MathCad program originating from the Liverpool group [7]. The Q-meter-based NMR system couples the target material to a sensing coil of intrinsic inductance L_0 . Whether the coil is wound around the sample or embedded within it, its bare inductance remains fixed. Introducing the sample alters the coil’s effective inductance through its magnetic susceptibility and coupling to the RF field, thereby shifting the circuit’s resonance. We can express this modified inductance of the combined sample–coil system as

$$L(\omega) = L_0(1 + 4\pi\eta\chi(\omega)) \quad (1)$$

where ω is the frequency probed at, η is the filling constant of the coil, and $\chi(\omega)$ is the complex RF susceptibility, which can be expressed as $\chi(\omega) = \chi'(\omega) - i\chi''(\omega)$. This complex RF susceptibility

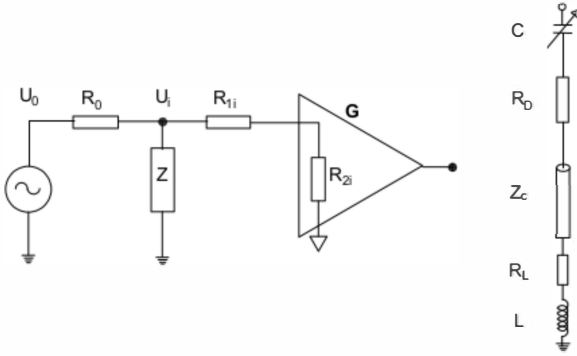


Fig. 1: Schematic of the Q-meter circuitry[27].

will only have non-zero values at frequencies near the resonant frequency of a target nucleon. The real part of the voltage across the Q-meter can be expressed as

$$\text{Re}\{u_i\} = \frac{U}{R_0} \left(\frac{\text{Re}\{Z\} + Y[\text{Re}^2\{Z\} + \text{Im}^2\{Z\}]}{[(1 + Y\text{Re}\{Z\})^2 + Y^2\text{Im}^2\{Z\}]} \right) \quad (2)$$

where $Y = \frac{1}{R_i} + \frac{1}{R_0}$ and is the coupling admittance of the resonator, R_i is the total impedance of the amplifier, which can be expressed as $R_i = R_{1i} + R_{2i}$ where R_{1i} is assumed to be purely resistive, R_0 is the current limiting resistance. A circuitry diagram of the Q-meter is shown in Fig. 1, where G is the amplifier gain, R_D is the damping resistance, C is the tuning capacitor, R_L is the inductive resistance, and Z_C is the impedance of the capacitor. In experiment, we set up the Q-meter to detect the real part of the target material's signal, so we must express the impedance of the resonant part of the circuit, Z_T , as

$$Z_T = R_D + \frac{1}{i\omega C} + Z_C \left(\frac{Z_L + Z_C \tanh \gamma l}{Z_C + Z_L \tanh \gamma l} \right), \quad (3)$$

where C is the tuning capacitor (a parameter we will discuss as C_{knob}), R_D is the damping resistor, Z_C is the conductor impedance, and Z_L is the impedance of the coil and l is the cable length defined by $n\lambda/2$ and n is an integer multiple providing the distance to the coil. We can express the coil impedance as

$$\begin{aligned} Z_L(\omega) &= R_L + i\omega L [1 + \eta_L(\chi'(\omega) - i\chi''(\omega))] \\ &= \frac{(R + i\omega L) \left(\frac{1}{i\omega C_{\text{stray}}} \right)}{(R + i\omega L) + \left(\frac{1}{i\omega C_{\text{stray}}} \right)}, \end{aligned} \quad (4)$$

where η_L is the filling factor, and $\chi(\omega) = \chi'(\omega) - i\chi''(\omega)$ is the complex magnetic susceptibility of the target material. In the second line, R denotes the effective series

resistance associated with the inductive branch of the resonant circuit, incorporating both the coil resistance and additional dissipative losses present at the coil terminals. The parameter C_{stray} represents the parasitic (stray) capacitance arising from the surrounding circuit environment. The impedance of the tuning capacitor is given by

$$Z_C(\omega) = \frac{1}{i\omega C(\omega)}. \quad (5)$$

We can then express the total impedance of the Q-meter system, $Z(\omega)$, as

$$Z(\omega) = \frac{R_1}{1 + \frac{R_1}{r + Z_C(\omega) + Z_T(\omega)}}, \quad (6)$$

where R_1 denotes the current-limiting (source) resistance of the RF drive stage, and r represents the remaining series resistance of the resonant circuit. The propagation constant of the $\lambda/2$ transmission line can then be expressed as

$$\begin{aligned} \gamma &= \sqrt{(R_c + i\omega L_c)(G_c + i\omega C_c)} \\ &\cong i\omega \sqrt{L_c C_c} \left(1 + \frac{1}{2iQ_c} \right). \end{aligned} \quad (7)$$

The characteristic impedance of the coaxial line is defined as

$$Z_c = \sqrt{\frac{R_c + i\omega L_c}{G_c + i\omega C_c}} \cong Z_0 \left(1 + \frac{1}{2iQ_c} \right), \quad (8)$$

where the subscript c specifically refers to parameters that are related to the $\lambda/2$, and $Z_0 = \sqrt{L_c/C_c}$ and $Q_c = \omega L_c/R_c$.

The Q-meter baseline curve was simulated by implementing this mathematical description of the Q-meter circuit [7] in various test configurations matched to experimental tests using a real Q-meter system. In doing this, we are able to adjust the simulation of the Q-meter system by adjusting 8 different simulated parameters that characterized the Q-meter RF circuitry and environment. These parameters are:

- C_{knob} : the tuning capacitance in the circuit. In practice, this parameter is adjusted by turning a variable capacitor knob on the Q-meter card. C_{knob} is adjusted such that the baseline curve is tuned. It has units of pF and typically ranges from 0.01 pF - 100 pF.
- U : input voltage. U is used to calculate the operating current through the Q-meter circuit via the equation $I = U/R$, the impedance $Z(\omega)$, and the phase $\phi(\omega)$, which leads to $V(\omega) = IZ(\omega)e^{i\phi(\omega)}$. It is in units of V and typically ranges from 0.1 – 1 V.
- $n/2$: the length of the $\lambda/2$ cable, also called the trim. We require that cable length be in discrete multiples of $\lambda/2$ in order for the circuit to be at resonant frequency ω_0 . This leads to the full length of the cable being $n\lambda/2$.

- η_L : filling factor of the coil. This factor is the level of coupling of spins in the target material to the sampling coil. It is unitless and ranges from 0 - 1.
- C_{stray} : Stray capacitance in the environment of the circuit including the parasitic capacitance between parts of an electronic component or circuit due to their close proximity. We can calculate the true capacitance of the LC circuit that's controlled by the variable capacitor knob to be

$$C(\omega) = k \times C_{knob} \quad (9)$$

The effective capacitance (including stray) can have a wide range of values, from a few to a few hundred pF, depending on the Larmor frequency.

- ϕ : Phase offset. We assume the form of the phase can be expressed as

$$\phi(\omega) = a\omega^2 + b\omega + \phi \quad (10)$$

where a and b are constants. Typically, this is within the range of $[0, 2\pi]$, but can extend beyond that in periodic cycles. A quadratic approximation is used to model the phase behavior within the waveguide. Higher-order terms are neglected because their contributions are small compared to other dominant sources of uncertainty and would be obscured by overlapping errors.

- L_0 : Coil Inductance. This is typically around the value of 50 mH and depends on the size of the NMR coil.
- DC Offset: This is used in the simulations to account for any physical DC offset that can't immediately be noticed from experimental measurements. Though it is usually pretty small, somewhere on the scale of $\approx 10^{-2}$ V, this can depend on the cable length.

Additionally, two slope terms are defined as:

$$\text{slope}_\phi = \frac{\delta\phi}{(\text{Sweep Length}) \times 2\pi \times 10^6}, \quad (11)$$

where $\delta\phi$ is a circuitry constant and "Sweep Length" is the amount of space one would like to cover given a point in a region of space. For instance, if the target sample is NH_3 , whose Larmor frequency is around 213 MHz at 5T, we can set this Sweep Length to be 4 MHz, assuming we are covering from 209 MHz - 217 MHz. We then define the phase of the signal going through the cable as,

$$\phi_{trim} = \text{slope}_\phi \times (\omega - \omega_0) + \phi(\omega). \quad (12)$$

where ω_0 is the resonant frequency being probed. Therefore, the total phase is defined as,

$$\phi(\omega)_{total} = \phi_{trim} + \phi. \quad (13)$$

So, we finally describe the output voltage of the Q-meter as

$$V_{out}(\omega) = \Re(I Z_{total}(\omega) e^{i\phi_{total}(\omega) \frac{\pi}{180}}) \quad (14)$$

where I denotes the RF drive current applied to the resonant circuit. Maintaining a constant drive current is essential, as the spin-transition rate and steady-state response depend on the RF field amplitude, which is directly proportional to I . Temporal variations in the applied current would lead to time-dependent excitation conditions, inducing nonuniform spin transitions and perturbing the spin population away from the desired steady state. The Q-meter-based NMR design therefore balances high-fidelity polarization measurement with minimal perturbation of the enhanced spin polarization, ensuring that the measurement remains effectively non-destructive.

Fig. 2 shows a simulation of the Q-meter baseline with a spin-1 TE signal lineshape and Gaussian noise produced by MC sampling. In our simulations we match the baseline parameters to realistic experimental scales as much as possible. Additionally, the scale of the baseline to signal is matched as is the signal-to-noise ratio. The top plot of the figure shows how small the TE signal is with respect to the scale of the baseline. A zoomed in view shows the two peaks of the Pake doublet of the simulated signal. The bottom plot shows the background subtracted zoomed in view.

2.2 Sources of Error

The standard Liverpool Q-meter system is susceptible to several distinct sources of noise and systematic uncertainty that can influence the observed NMR signals. These contributions originate from power delivery and grounding, mechanical and electrical connectivity, the surrounding RF environment, and the intrinsic noise properties of the readout electronics. Collectively, they can introduce both stochastic noise and structured distortions into the measured spectra.

At the front end of the system, thermal noise generated by resistive elements in the resonant circuit, cabling, and preamplifier input stages contributes additive noise that is well approximated by Gaussian statistics. While this noise is often treated as spectrally white at the point of generation, it can become frequency dependent after passing through the resonant tank circuit, band-limiting filters, and frequency-dependent gain of the Q-meter chain, which can result in colored Gaussian noise in the measured spectrum.

Additional noise contributions arise from the RF environment and power infrastructure. Imperfect

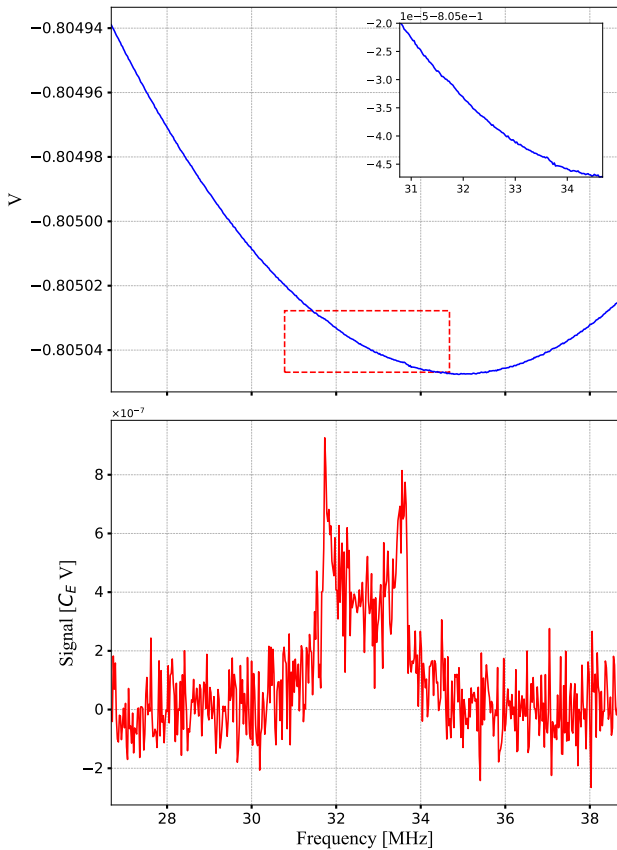


Fig. 2: Top: Example of a simulated Q-meter baseline containing a deuteron NMR lineshape at 0.05% polarization (TE), with MC Gaussian noise added at a signal-to-noise ratio of 2.6. For clarity, the signal shown in the inset is scaled by a factor of 10^2 . Bottom: The same signal as in the top panel, shown after baseline subtraction and magnified for visibility.

grounding, ground loops, and power-supply ripple can introduce coherent or quasi-coherent interference at specific frequencies, leading to narrowband noise or baseline modulation. External RF pickup, including environmental electromagnetic interference and cross-coupling from nearby RF systems, can further contaminate the signal with non-white and, in some cases, non-Gaussian components.

Mechanical factors such as loose connections, cable motion, and microphonics can modulate impedance and phase in the resonant circuit, producing low-frequency fluctuations and baseline instabilities that are correlated across frequency bins. These effects are not well described by ideal white-noise assumptions and can introduce structured distortions that persist across repeated measurements.

Finally, digitization and signal processing steps—including mixing, demodulation, filtering, and

baseline subtraction—can reshape both the amplitude distribution and spectral content of the noise, further complicating its characterization. As a result, the noise observed in the final NMR spectra is generally a superposition of Gaussian and non-Gaussian components with frequency-dependent structure, rather than purely additive white Gaussian noise.

The more the environmental noise conditions can be studied the better it can be simulated. For our basic benchmark studies we focus on the largest scale standard contributions that can alter the shape, stability, or interpretation of the resulting NMR signals with the understanding that additional contributions can easily be added for specific environments. We include just the most basic noise and baseline systematics:

- **Gaussian Noise:** This is effectively purely ‘background’ noise that is witnessed in every bin across all the recorded NMR data. This type of noise is suppressed (averaged out at $1/\sqrt{N}$) for increased number of NMR sweeps (N).
- **Sinusoidal Noise:** Dirty sources of power for the Q-Meter system can lead to sinusoidal-type interference showing up as both regular and irregular noise. This type of noise is generally suppressed with high number of sweeps (5000) during baseline measurements, assuming its unchanged over time.
- **Shifts in Baseline:** This effect typically manifests as a sudden shift in the tuning condition resulting in a skewed or tilted baseline. Such shifts can arise from several sources, including spontaneous changes in tuning due to loose $\lambda/2$ or phase-cable connections, temperature-induced drift within the system, or variations in capacitance between the LC tank circuit and the phase detector. Any of these mechanisms can perturb the balance of the resonant circuit and introduce a persistent baseline distortion in the measured spectrum.

Beyond these contributions, there is significant fitting error from standard extraction methods that are not encoded in the simulations but are worth mentioning here. Time-dependent variations in the measured Q-curve or NMR signal, as well as imperfect baseline subtraction, can introduce a residual background in the spectrum. Traditional analysis methods attempt to remove this contribution by fitting and subtracting a low-order polynomial—typically third order, and in some cases second order—to the spectral wings. When this procedure is inadequate, the remaining background can distort the extracted NMR signal, leading to a systematic bias. This effect constitutes a baseline-induced fit error rather than statistical (Gaussian) noise. When using Dulya type fitting [9, 15] off-center fits or poor baseline subtraction can result in false asymmetry in the two absorption intensities.

Additionally, when calibration constants are used to map the integrated NMR area to polarization—most notably for the proton—the uncertainty in the extracted calibration constant obtained from the TE measurement can be dominated by large-scale noise relative to the signal amplitude. This effect can lead to a substantial relative uncertainty in the extracted polarization. Further contributions may arise if the spin system has not fully reached true thermal equilibrium at the time of calibration; however, this constitutes a systematic effect that is not addressed in the present work. The signal-to-noise limitations of TE measurements, along with the other error sources listed above, can be reliably modeled within the simulation framework employed here.

Specific DNN models can be trained using the simulated data to predict either the signal area or the polarization directly. The area-based approach is more general and can be applied to both spin-1/2 and spin-1 systems. In contrast, direct polarization prediction is best suited to spin-1 targets in materials with non-cubic symmetry, where each polarization value produces a distinct lineshape. For the direct polarization case, our first step is to leverage the lineshape theory of the spin-1 system as part of the training information to be able to directly determine polarization in a range of noisy or baseline distorted conditions.

3 Spin-1 Lineshape Theory

3.1 Polarization of Spin-1 Materials

When a spin-1 target material is placed in an external magnetic field \vec{B} , its nuclear spin states undergo Zeeman splitting into three levels E_m with $m = 0, \pm 1$. Spin-1 nuclei additionally interact with local electric field gradients (EFGs), which generate a nuclear quadrupole moment and further modify the level structure. The size of this quadrupole interaction depends on both the applied field strength and the surrounding crystalline environment, and for sufficiently strong fields (~ 5 T) it enters as a small perturbation to the dominant Zeeman term.

The most common spin-1 target materials are ND_3 and deuterated butanol with nuclei of interest being normally ^2H or ^{14}N where the lack of cubic symmetry in the material crystal lattice leads to nonzero EFGs that couple to the quadrupole moment. This coupling lifts the degeneracy of the Zeeman-split states in an asymmetric fashion, yielding two partially overlapping absorption lines in the NMR spectrum. The resulting energy levels for

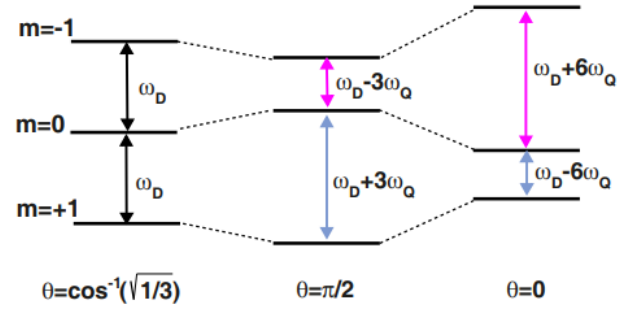


Fig. 3: Energy level structure of deuterium in a magnetic field of strength B . The splitting includes both Zeeman and quadrupole contributions. Pink lines denote transitions $-1 \leftrightarrow 0$ and blue lines denote $0 \leftrightarrow +1$ [17].

such systems can be written as [1, 9]

$$E_m = -\hbar\omega_0 m + \hbar\omega_Q [3 \cos^2(\theta) - 1 + \eta \sin^2(\theta) \cos(2\phi)] (3m^2 - 1), \quad (15)$$

where $m = 0, \pm 1$ is the magnetic quantum number, θ and ϕ are the polar and azimuthal bond angles with respect to the magnetic field, η is the asymmetry parameter, ω_0 is the Zeeman/Larmor frequency, and ω_Q is the quadrupole frequency proportional to the EFG strength. These transitions are shown in Fig. 3. The allowed NMR transitions $E_0 \leftrightarrow E_{\pm 1}$ occur at two distinct resonant frequencies, corresponding to intensity functions $I_{\pm}(R)$ parametrized by the dimensionless frequency variable

$$R = \frac{\omega - \omega_0}{3\omega_Q},$$

where ω is the probe frequency. The resonant energies are given by

$$\Delta E_{\pm} = \hbar\omega_{\pm} \mp 3\hbar\omega_Q \{ [3 - \eta \cos(2\phi)] \cos^2(\theta) - [1 - \eta \cos(2\phi)] \}. \quad (16)$$

The angle θ at which a given resonance occurs can be expressed in closed form as

$$\cos(\theta, \varepsilon) = \sqrt{\frac{1 - \varepsilon R - \eta \cos(2\phi)}{3 - \eta \cos(2\phi)}}, \quad \varepsilon = \pm 1. \quad (17)$$

Each branch of ε corresponds to one of the two absorption lobes of the deuteron NMR doublet. A full model must also account for dipolar broadening arising from spin-spin interactions, which produces a Lorentzian distribution in ω_0 and leads to the convolution integral [9]:

$$\begin{aligned}
f_\varepsilon(R, A, \eta, \phi) &= \int_{2\varepsilon}^{\varepsilon[1-\eta\cos(2\phi)]} \frac{1}{y} \frac{A/\pi}{A^2 + \varepsilon^2(x-R)^2} d(\varepsilon x) \\
&= \frac{2A}{\pi} \int_0^{\mathcal{Y}} \frac{d\mathcal{X}}{\mathcal{X}^4 - Q^2\mathcal{X}^2 + A^2 + Q^4},
\end{aligned} \tag{18}$$

where

$$\mathcal{X} = \sqrt{1 - \varepsilon x - \eta \cos(2\phi)}, \tag{19}$$

$$\mathcal{Y} = \sqrt{3 - \eta \cos 2\phi}, \tag{20}$$

$$Q = \sqrt{1 - \varepsilon R - \eta \cos(2\phi)}, \tag{21}$$

and $f_\varepsilon(R, A, \eta, \phi)$ represents the normalized absorption intensity associated with a single branch of the quadrupole-split deuteron NMR line as a function of the reduced detuning parameter R , the dipolar broadening parameter A , the quadrupole asymmetry parameter η , and the azimuthal angle ϕ .

The resulting analytical lineshape (intensity) from Eq. 18 after integration is [1, 9]

$$\begin{aligned}
I(R, \varepsilon) &= \frac{1}{2\pi\mathcal{X}} \left[2\cos\left(\frac{\alpha}{2}\right) \left(\arctan\left(\frac{\mathcal{Y}^2 - \mathcal{X}^2}{2\mathcal{Y}\mathcal{X}\sin(\frac{\alpha}{2})}\right) + \frac{\pi}{2} \right) \right. \\
&\quad \left. + \sin\left(\frac{\alpha}{2}\right) \ln\left(\frac{\mathcal{Y}^2 + \mathcal{X}^2 + 2\mathcal{Y}\mathcal{X}\cos(\frac{\alpha}{2})}{\mathcal{Y}^2 + \mathcal{X}^2 - 2\mathcal{Y}\mathcal{X}\cos(\frac{\alpha}{2})}\right) \right],
\end{aligned} \tag{22}$$

with

$$\mathcal{X} = \sqrt{\Gamma^2 + (1 - \varepsilon R - \eta \cos 2\phi)^2}, \tag{23}$$

$$\cos \alpha = \frac{1 - \varepsilon R - \eta \cos 2\phi}{\mathcal{X}}. \tag{24}$$

The full deuteron NMR absorption lineshape is the sum $I_+(R) + I_-(R)$, with peaks at $R = \pm 1$, reflecting the angular condition for maximum perpendicularity between the RF field and nuclear magnetic axis. An example simulated lineshape is shown in Fig. 4.

Vector and Tensor Polarization

For a spin-1 system with sublevel populations n_{+1} , n_0 , and n_{-1} , the vector (nuclear) and tensor (quadrupole) polarizations are defined as,

$$P_n = \frac{n_{+1} - n_{-1}}{n}, \tag{25}$$

$$Q_n = \frac{n - 3n_0}{n}, \tag{26}$$

where

$$n \equiv n_{+1} + n_0 + n_{-1} = 1. \tag{27}$$

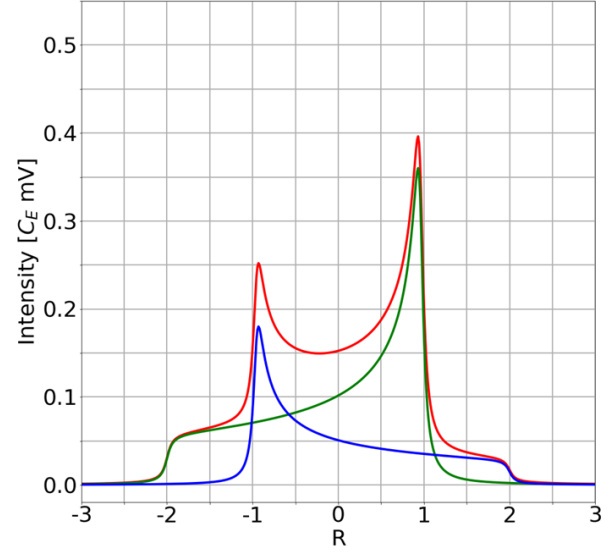


Fig. 4: Simulated deuteron absorption lineshape showing I_+ (green) and I_- (blue) solutions. The horizontal axis is the dimensionless detuning parameter R .

Where under Boltzmann equilibrium conditions the tensor polarization can be expressed as,

$$Q_n = 2 - \sqrt{4 - 3P_n^2}. \tag{28}$$

The lineshape integrals provide the link between measured intensity and polarization [15]:

$$P(R) = C(I_+(R) + I_-(R)), \tag{29}$$

$$Q(R) = C(I_+(R) - I_-(R)), \tag{30}$$

where C is a calibration constant. A commonly used alternative formulation introduces the ratio

$$r = \frac{I_+}{I_-},$$

yielding the vector polarization expression [9]

$$P = \frac{r^2 - 1}{r^2 + r + 1}. \tag{31}$$

This formula is advantageous in simulation-based machine learning studies, as synthetic datasets may be generated by selecting a target polarization, computing r , and then constructing I_\pm accordingly. We note here that the Boltzmann constraint need not be enforced when using Eq. 29 and 30 [15] which allows the two absorption areas to vary independently. For simplicity, we maintain the Boltzmann constraint in our simulations.

3.2 Materials with Cubic Symmetry

Some spin-1 target materials, such as ${}^6\text{LiD}$, place the spin-1 nucleus in an approximately cubic crystal field. In ${}^6\text{LiD}$, the relevant spin may be either the ${}^6\text{Li}$ or deuteron nucleus, both of which have nuclear spin $I = 1$. In a general crystalline environment, the nuclear electric quadrupole moment couples to the local EFG, described by the second-rank tensor $V_{ij} \equiv \partial^2 V / \partial x_i \partial x_j$, where V is the electrostatic potential at the nuclear site. This quadrupole interaction lifts the degeneracy of the $m = \{-1, 0, +1\}$ Zeeman sublevels and splits the allowed $m = -1 \rightarrow 0$ and $m = 0 \rightarrow +1$ transitions, producing a characteristic quadrupolar doublet in the NMR spectrum (Fig. 4) rather than a single resonance.

In a cubic or nearly cubic environment, however, the principal components of the EFG tensor satisfy $V_{xx} \approx V_{yy} \approx V_{zz}$, causing the traceless quadrupole interaction to be strongly suppressed at the nuclear site. In this limit, the nuclear-spin Hamiltonian is dominated by the Zeeman term, and the transition energies for the $m = -1 \rightarrow 0$ and $m = 0 \rightarrow +1$ transitions become degenerate, both occurring at $\hbar\omega_0 = \gamma\hbar B_0$. As a result, the two transitions contribute to a single unresolved resonance, and the ${}^6\text{Li}$ (or deuteron) NMR response in ${}^6\text{LiD}$ appears as a single proton-like peak rather than a quadrupole-split doublet.

The resulting line shape is well modeled by a Voigt profile, i.e. a convolution of Gaussian and Lorentzian contributions,

$$f(x; \sigma, \gamma) \equiv \int_{-\infty}^{\infty} G(x'; \sigma) L(x - x'; \gamma) dx', \quad (32)$$

where G and L denote the Gaussian and Lorentzian distributions, respectively [1]. The Gaussian component arises from static or quasi-static inhomogeneities in the local magnetic field experienced by each nucleus. In both proton targets such as NH_3 (where the relevant nuclei are spin-1/2 protons) and spin-1 targets such as ${}^6\text{LiD}$, the nuclei are embedded in a rigid lattice and are subject to a distribution of dipolar fields from neighboring spins, small variations in bulk susceptibility and demagnetization fields, and, in some cases, chemical-shift dispersion. Because these contributions are the sum of many small, randomly distributed interactions, the distribution of resonance frequencies is well approximated by a Gaussian. This inhomogeneous broadening mechanism is essentially the same for the proton spins in NH_3 and for the ${}^6\text{Li}$ spins in ${}^6\text{LiD}$ once the quadrupole interaction of the latter is quenched by cubic symmetry, so the observed line shapes are qualitatively similar.

The Lorentzian part of the Voigt profile represents homogeneous broadening mechanisms that affect all spins more uniformly. These include spin-spin relaxation

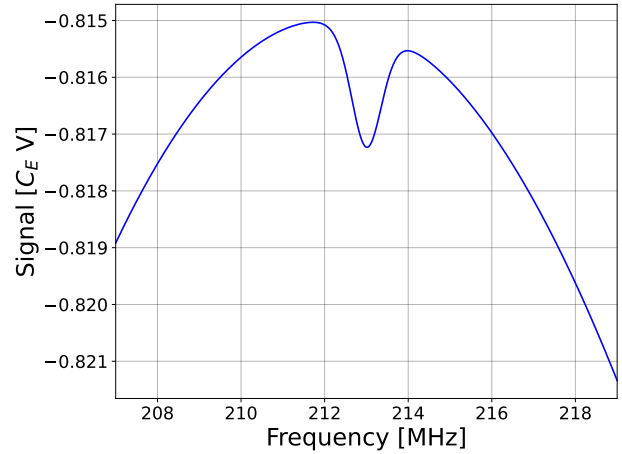


Fig. 5: Simulated proton NMR signal demonstrating a Voigt type lineshape. Parameters for Voigt profile simulation were extracted from experimental fits.

characterized by the nuclear transverse relaxation rate T_2 , the decay time constant associated with the spin-spin relaxation time. This relaxation produces exponential dephasing of the transverse magnetization, and additional time-dependent local field fluctuations such as those induced by residual molecular motion, spin diffusion, or electron-nuclear interactions in dynamically polarized targets [2]. Under strong microwave irradiation for dynamic nuclear polarization, power broadening of the coupled electron-nuclear system can further increase the Lorentzian width. In CW-NMR the observed single line for both proton and spin-1 signals therefore has a total width determined by the combination of static dipolar and susceptibility inhomogeneities (encoded in the Gaussian width σ) and homogeneous relaxation and power broadening (encoded in the Lorentzian width γ). For spin-1 targets like ${}^6\text{LiD}$ with cubic symmetry, the absence of a resolved quadrupolar splitting means that these same mechanisms dominate the line shape, making the spin-1 signal closely resemble the proton signal displayed in Fig. 5.

With these details in mind, we can reduce our overall simulation suite to focus primarily on two types of lineshapes: the Pake doublet (lineshape approach) and the Voigt (area focused approach). With these two we can essentially simulate all popular polarized target signal types.

4 Methodology for Extraction of Polarization

In this section we will review the traditional polarization extraction techniques, such as the thermal equilibrium

measurements and lineshape fitting. We then introduce the DNN approaches.

4.1 Thermal Equilibrium Technique

The first of the traditional polarization measurement techniques is the area-based calibration method, which relies on a thermal-equilibrium (TE) measurement to establish an absolute normalization relating the integrated NMR signal area to the polarization (vector polarization in the case of spin-1 targets). When the lattice and target material are allowed to reach true thermal equilibrium, the resulting polarization is uniquely determined by the spin quantum number and follows the well-defined Boltzmann distributions for spin-1/2 and spin-1 systems:

$$P_{\text{TE}}^{S=\frac{1}{2}} \approx \tanh\left(\frac{g\mu B}{2kT}\right), \quad (33)$$

$$P_{\text{TE}}^{S=1} \approx \frac{4}{3} \tanh\left(\frac{g\mu B}{2kT}\right). \quad (34)$$

where B is the external magnetic field, μ the magnetic moment in the external field of strength B , k is the Boltzmann constant, g is the g-factor of the specimen, and T is the temperature of the system [8].

A typical calibration temperature of $T = 1.5$ K, with NH_3 as an example, this yields a reference polarization of

$$P_{\text{TE}}^{S=\frac{1}{2}} \approx 0.34\%. \quad (35)$$

and for ND_3 ,

$$P_{\text{TE}}^{S=1} \approx 0.053\%. \quad (36)$$

Once this reference value is established, any non-equilibrium polarization can be determined by integrating the measured absorption signal [9],

$$P = C \int \frac{d\omega S(\omega)}{\omega}, \quad (37)$$

where $S(\omega)$ denotes the extracted NMR absorption signal as a function of angular frequency. In the context of a Q-meter-based CW-NMR measurement, this signal is defined as

$$S(\omega) \equiv \Re\{V(\omega, \chi) - V(\omega, 0)\} \propto \chi''(\omega), \quad (38)$$

with $V(\omega, \chi)$ the measured complex voltage across the resonant circuit in the presence of nuclear susceptibility $\chi(\omega)$, and $V(\omega, 0)$ the corresponding background voltage measured in the absence of the NMR response. The quantity $\chi''(\omega)$ is the absorptive component of the complex magnetic susceptibility, which carries the polarization-dependent signal. The proportionality

constant C is a calibration factor determined from the thermal-equilibrium measurement and provides the absolute normalization relating the integrated signal area to the physical polarization.

The constant C is obtained directly from a TE calibration measurement via,

$$C = \frac{P_{\text{TE}}}{\int \frac{d\omega S(\omega)}{\omega}}, \quad (39)$$

where P_{TE} is the TE polarization of either a spin-1/2 or spin-1 sample and T taken as the experimentally measured lattice temperature [8].

The thermal-equilibrium (TE) calibration method can introduce substantial uncertainty, resulting in a total error of 3–5% relative for proton polarization under realistic experimental conditions [15]. For spin-1 targets, the corresponding uncertainty is generally larger; moreover, even a vector-polarization uncertainty of this magnitude propagates to a relative uncertainty exceeding 7% in the extracted tensor polarization [17, 16, 18, 24] when using the standard Boltzmann relationship in Eq. 28. Such deviations commonly arise from a limited number of TE calibration points or from insufficient time for the target material to reach true thermal equilibrium. In practice, when relying on the TE method, these sources of uncertainty are often unavoidable due to beam-time constraints and operational priorities. By contrast, the uncertainty component arising purely from spectral fitting and area integration is typically at the 2–3% level [16], representing the dominant avenue where methodological improvements can be achieved.

4.2 Dulya (and Dulya-Like) Fitting

For spin-1 targets with non-cubic symmetry a lineshape fitting method can be used such as the Dulya method [9] and Dulya-like fits [15] involving the use of an analytical lineshape formula (Eq.22)—to fit directly to the NMR signal. Usually, one subtracts the baseline and fits a parabolic curve to the residual background and subtracts it out to remove the Q-Curve similar to the area approach. One can also fit without baseline subtraction. Then, a χ^2 minimization fit is done using Eq.22 to extract the intensity ratio of I_+ and I_- . The fitted absorption lines heights are used to find the ratio of the peaks (or ratio of the absorption line areas in similar methods [15]), r , and calculate the vector polarization via Eq. 31. The relative error of the lineshape-based approach is generally smaller for spin-1 systems than that of the TE method, primarily because the TE-area is typically very small, resulting in reduced signal-to-noise. In contrast, fitting the full lineshape yields a more accurate determination of the

polarization and does not require waiting for the target to thermalize.

4.3 Artificial Neural Networks (ANN)

Neural networks are trained by repeatedly presenting labeled examples—each consisting of an input and its corresponding output—and adjusting internal parameters to strengthen the mapping between them. Through this iterative optimization, the model encodes a probability-weighted representation of the underlying functional relationship within its parameters. While the literature on artificial neural networks (ANNs) is vast, we provide only a concise overview here.

A neural network may be viewed as a composition of nonlinear functions—commonly referred to as *activation functions*—denoted by ϕ_i . For a given network architecture, one constructs a sequence of transformations

$$\phi_1, \phi_2, \dots, \phi_L$$

whose composition aims to approximate a target function \hat{f} according to an optimization criterion, typically defined by a loss function [11]. The Universal Approximation Theorem guarantees that, under mild assumptions, sufficiently large networks can approximate any continuous function \hat{f} to arbitrary precision ε [13]. However, the theorem is non-constructive: it does not specify the required architecture, depth, width, or choice of nonlinearities.

In practice, network accuracy depends sensitively on *hyperparameters*—including depth, width, learning rate, regularization, and activation type—which must be tuned for the problem at hand. Training proceeds by forward-propagating an input through the network to produce a prediction, comparing that prediction to the target output via the loss function, and then updating the network weights through backpropagation. Repeating this process over many examples iteratively reduces the loss, yielding a model whose outputs converge toward the desired target values.

Inspired by data augmentation methods commonly used in computer vision [19, 29], we introduced controlled transformations to the simulated baseline signals in diode mode of the Q-meter, shown in Fig. 6. These baseline shifts arise from small perturbations in three physical parameters of the Q-curve model: the applied voltage U , the adjustable capacitance $C_{\text{kno}}b$, and the phase φ . Let $x \in \mathcal{D}$ denote a clean, simulated signal prior to augmentation. We define an augmentation operator

$$T_{\theta}(x) = x + g(U + \Delta U, C_{\text{kno}}b + \Delta C, \varphi + \Delta \varphi), \quad (40)$$

where $\theta = (\Delta U, \Delta C, \Delta \varphi)$ represents small, physically realistic perturbations sampled from bounded

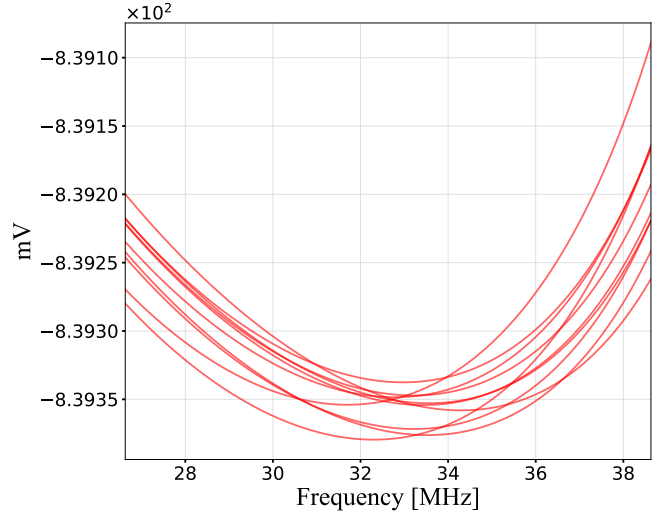


Fig. 6: Examples of applied variations in the simulated baseline in diode mode.

distributions, and $g(\cdot)$ represents the baseline-shape generating function of the circuit model. The augmented dataset is then

$$\tilde{\mathcal{D}} = \{T_{\theta}(x) \mid x \in \mathcal{D}, \theta \sim P(\theta)\}. \quad (41)$$

As an example of variation with the deuteron 5 T cable length set to one $\lambda/2$, U is varied between 0.001 - 1V, while $C_{\text{kno}}b$ is varied between 0.150 - 0.300 pF, and phase is varied at $\pm 20\%$ from its optimal tune (2π). We note that phase changes affect the signal characteristics as well, which are a critical part of the training to make the model more generally robust to unintended tune shifts.

The motivation for this augmentation strategy is two-fold. First, it increases the effective sample size $|\tilde{\mathcal{D}}|$, which is known to reduce overfitting and improve generalization bounds through variance reduction in empirical risk minimization [32, 36]. Second, it expands the functional variability of the data distribution, thereby increasing the diversity of the hypothesis space the model must approximate. Formally, if \mathcal{F} denotes the class of real-valued measurable functions capable of mapping signals to polarization values, i.e.,

$$\mathcal{F} : \tilde{\mathcal{D}} \rightarrow \mathbb{R}, \quad (42)$$

then augmentation can be viewed as broadening the support of the empirical data distribution toward the true underlying generative distribution encountered in real measurements. This reduces covariant shift and improves robustness under domain variability [10].

The simulated lineshape of the signal is characterized by extracting the lineshape parameters using the standard fitting procedures [15, 9] to experimental data. The

parameterized simulated signal is added to the simulated Q-curve, along with various types of noise to make high-quality training and test data.

The applied controlled transformations are intended to replicate realistic environmental effects in the Q-curve and signal, accounting for phase shifts that produce lineshape distortions associated with the dispersive response of the signal, in addition to systematic modifications to the spectral baseline. Additionally, the simulated noise described in Sec. 2.2 is injected at various scales during training to mimic realistic scenarios and further generalize lineshape features.

In short, by incorporating realistic noise and physical perturbations of baseline and tune parameters, our augmentation approach increases the representational richness of the dataset and enhances the model’s capacity to generalize to unseen experimental signals rather than memorizing parametrically constrained simulated profiles.

We trained four separate neural network models:

1. a polarization model for the 2%–60% polarization region (hereafter referred to as the “*high-polarization model*”),
2. a polarization model for the 0–2% polarization region (hereafter referred to as the “*low-polarization model*”),
3. an area-prediction model (“*area model*”) targeting the 0–100% range, with particular emphasis near the TE region for the proton.
4. a denoising autoencoder design (DAE) to filter out noise from signal data.

For the high-polarization model, the lower bound of 2% is chosen because the lineshape continues to exhibit a clearly quantifiable asymmetry between the two absorption lines, which remains discernible even in the presence of moderate noise. The upper bound of 60% reflects the typical polarization range of our case study; however, the model can be straightforwardly extended to 100% polarization by incorporating additional training data at higher polarization values. Overall performance is discussed in Sec. 6.

A separate low-polarization model is required because polarization extraction in this regime constitutes a fundamentally different inference problem. At polarization levels approaching 0.05%, the signal becomes strongly noise-dominated, imposing severe limitations on lineshape-based extraction. Alongside limitations from very low SNR, signal-to-baseline ratios also become vanishingly small. This in turn can lead to a severe underperformed in feature learning and extraction for neural network models due to the relatively small scale of pertinent features. This limitation motivated a very careful handling of training data generation mimicking the 50 gain setting on the Q-meter and ensuring consistent the baseline

scale and relative signal magnitude. This allows the relative size (magnified by 50) with respect to the baseline as the dominant training feature at the cost of broader generalization. This is effectively equivalent to inferring the polarization from the signal area in conjunction with the signal lineshape information leading to improved results discussed in Sec. 6.

The area model is designed to work with any signal lineshape and would generally be required for proton type signals and other spectra that do not require a specific lineshape for accurate inference. Since the low polarization model is designed to work for the TE range of the Pake doublet type of spin-1 signal the area model focuses on proton scale TE which makes it a much simpler model in general only needed a quality extraction of signal areas that correspond to 0.3% polarized.

Finally, the DAE serves a distinct role from the other models: its primary purpose is to suppress noise in the NMR signal, rather than to directly infer polarization values. The cleaned signal can then be better analyzed with other tools to evaluate the spectra or polarization.

4.4 Analysis Metrics

To evaluate model performance, we employ several quantitative metrics, the results of which are presented in Sec. 6. Model performance is characterized in terms of the mean residual (bias), accuracy, and precision, as defined below.

For each test sample, we define the pointwise residual as

$$\text{res}_n = \text{True}_n - \text{Predicted}_n, \quad (43)$$

where True_n denotes the known simulated value from the test dataset and Predicted_n is the corresponding model output. The mean residual, which quantifies the systematic bias of the model, is then given by

$$\langle \text{res} \rangle = \frac{1}{N} \sum_{n=1}^N \text{res}_n. \quad (44)$$

Using the pointwise residuals, we define the model accuracy as the mean absolute fractional deviation between the predicted and true values,

$$\text{Accuracy} = \left(1 - \frac{1}{N} \sum_{n=1}^N \left| \frac{\text{res}_n}{\text{True}_n} \right| \right) \times 100\%, \quad (45)$$

where N is the total number of test samples.

Model precision is quantified by the width of the residual distribution, taken as the standard deviation σ of the pointwise residuals across the test dataset. Under this definition, smaller values of σ correspond to higher model

precision, reflecting a narrower distribution of prediction errors.

Noise levels for each event were quantified using the signal-to-noise ratio (SNR), defined as

$$\text{SNR} = \frac{\max(|\text{Signal}|)}{\max(|\text{Noise}|)}. \quad (46)$$

An SNR value of 1 indicates that the noise amplitude is equal in magnitude to the signal amplitude. Values significantly greater than 1 correspond to comparatively low-noise events, while values much less than 1 indicate highly noise-dominated events. In this context, the “signal” refers specifically to the ND₃ lineshape, excluding the baseline contribution, as shown in Fig. 2. This definition of SNR provides a more realistic representation of the noise scale relative to the physical lineshape, particularly in regions near the thermal-equilibrium (TE) polarization limit.

5 Model Construction

To address the distinct inference tasks associated with polarization extraction, signal-area determination, and noise suppression, we employ a suite of specialized neural network architectures. Convolutional neural networks (CNNs) are used for both the high- and low-polarization models, where localized spectral features and lineshape asymmetries carry the dominant physical information. A simpler multilayer perceptron (MLP) architecture is adopted for the area model, for which global amplitude information is sufficient and explicit spatial feature extraction is not required. In addition, a denoising autoencoder (DAE) is employed to suppress stochastic noise and recover clean spectral structure prior to downstream analysis. In the following subsections, we describe the architecture, training strategy, and intended role of each model in detail.

5.1 Polarization Models

We approached the polarization and signal-extraction problem using a CNN [20], a class of feed-forward neural networks trained via gradient-based optimization of convolutional kernels. CNNs are widely employed in modern machine learning—particularly in computer vision, image analysis, and spatiotemporal signal processing—due to their parameter efficiency, translation-equivariant structure, and strong inductive biases toward local feature extraction.

In the context of CW-NMR spectra, these properties are especially well matched to the underlying physics of the signal. The relevant information is encoded in

localized spectral features—such as peak structure, relative lobe asymmetry, linewidth, and baseline curvature—that are largely invariant under small frequency shifts and scale changes induced by tuning drift, phase offsets, or baseline distortions. Convolutional kernels naturally capture such local correlations while remaining insensitive to their absolute position in frequency space, making CNNs well suited for robust polarization inference under non-ideal experimental conditions.

Furthermore, the implicit regularization introduced by convolutional weight sharing substantially reduces the number of free trainable parameters relative to fully connected architectures. This improves generalization, reduces overfitting, and mitigates training instabilities such as vanishing or exploding gradients [34]. Taken together, these characteristics make CNN-based architectures a natural and physically motivated choice for extracting polarization and signal observables from noisy, baseline-distorted NMR spectra.

A core architectural component of our model is the use of residual connections. Residual connections (or residual blocks) enable direct signal pathways within deep networks, improving gradient flow during backpropagation and allowing substantially deeper architectures to be trained without degradation [12]. A residual block takes an input x and outputs

$$\text{ResBlock}(x) = F(x) + x, \quad (47)$$

where $F(\cdot)$ is a learnable nonlinear transformation (typically a composition of convolution, normalization, and activation layers). In the original formulation of [12], the underlying mapping $H(x)$ is expressed as $H(x) = F(x) + x$, where $F(x) := H(x) - x$ is known as the *residual function*. An example figure of a ResBlock is shown in Fig. 7. The use of residual connections is now ubiquitous in modern deep learning due to demonstrated improvements in stability, convergence, and predictive performance across domains.

We also incorporated a multi-scale convolution blocks—also known as an *Inception Block* [31]—, designed to (1) leverage convolutions across multiple scales of spatial information and (2) reduce model complexity while increasing performance. The basic premise, as described in [31], involves several independent convolutions on an input which are then concatenated. As a preliminary step, we decided to attempt this problem with just one block after the initial layer. However, more sophisticated models can include several or even dozens within an architecture.

Finally, prior to global pooling, we incorporate a *squeeze-and-excitation (SE) block*, inspired by the framework introduced in Squeeze-and-Excitation Networks [14]. Consider a transformation \mathbf{T} that maps an

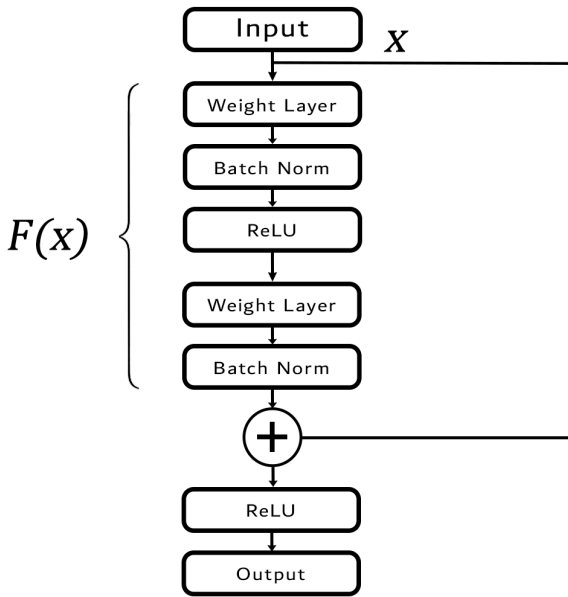


Fig. 7: Example architecture of Residual Block (ResBlock).

input \mathbf{X} to a set of feature maps $\mathbf{U} \in \mathbb{R}^{H \times W \times C}$, where H , W , and C denote the spatial dimensions and number of channels produced by a convolutional operation. An SE block adaptively recalibrates these feature maps by explicitly modeling channel-wise interdependencies, thereby enhancing representational capacity and overall model performance.

The *squeeze* operation performs global average pooling across the spatial dimensions $H \times W$, generating a compact channel descriptor that captures the global distribution of feature responses. This is followed by an *excitation* operation, which maps the channel descriptor to a set of per-channel modulation weights. These weights are then applied to \mathbf{U} via channel-wise scaling, producing the output of the SE block, which is subsequently passed to downstream layers of the network. In practice, this self-gating mechanism is akin to a computationally efficient attention mechanism, which weights relevant information within feature maps [14, 33]. Fig. 8 shows a high-level diagram of the CNN-based architecture used to build the polarization models.

Although the high- and low-polarization models share an identical architectural layout and block structure—including the use of specialized Inception-style modules and SE blocks—their optimization procedures were performed independently. As a result, differences in the optimized filter depths, channel widths, and regularization parameters led to distinct effective parameterizations and, consequently, different numbers of free trainable parameters in each model.

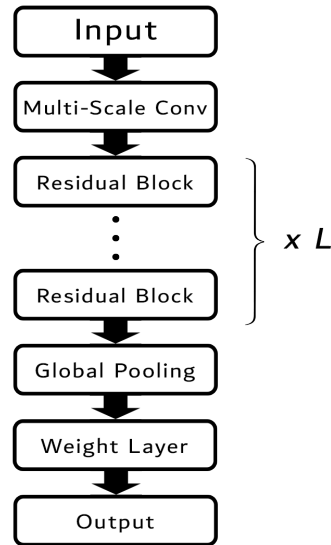


Fig. 8: Abstract Architecture Diagram of model used for both CNN-based polarization and area models. Hyperparameters varied between each model.

Hyperparameter	Value
Layer_1 Neurons	500
Layer_2 Neurons	32
Layer_3 Neurons	32
α (Learning Rate)	1.0×10^{-3}
Batch Size	256
ϵ	1.0×10^{-7}
β_1	0.9
β_2	0.999
clipnorm	1.0

Table 1: Tuned hyperparameters for the dense feed-forward model.

Hyperparameter	Value
# of Residual Blocks	4
Filters per Layer	64
α (Learning Rate)	0.0081694
Batch Size	256
Momentum	0.9538
ϵ	3.6438×10^{-5}
β_1	0.2936
β_2	0.2334
clipnorm	4.9805

Table 2: Tuned hyperparameters for the Polarization model.

Tables 1 and 2 summarize the optimized hyperparameter configurations (selection for these choices are discussed in sec. 5.4). The hyperparameters ϵ , β_1 , β_2 , α , and clipnorm correspond to components of the AdamW optimizer [22], a decoupled variation of Adam that separates L_2 -based weight decay regularization from gradient-based updates. Here, ϵ is a small constant added

to the denominator for numerical stability, while β_1 and β_2 are exponential decay coefficients for the first- and second-order moment estimates of the gradient, respectively. With initial learning rate α and weight-decay parameter λ , the parameter update rule is

$$\theta_{t+1} = \theta_t - \alpha \left(\frac{\hat{m}_t}{\sqrt{\hat{v}_t + \varepsilon}} + \lambda \theta_t \right), \quad (48)$$

where \hat{m}_t and \hat{v}_t are the bias-corrected estimates of the first and second moments of the gradient. We used the learning rate scheduler `CosineAnnealingWarmRestarts` [26], which progressively adjust the learning rate during training as

$$\alpha_t = \alpha_{\min} + \frac{1}{2} (\alpha_{\max} - \alpha_{\min}) \left(1 + \cos \left(\frac{T_i}{T_{\text{cur}}} \pi \right) \right). \quad (49)$$

where α_{\max} is the initial learning rate, T_{cur} is the number of epochs since the last restart, and T_i is the period—or, number of epochs between two warm restart in stochastic gradient descent with warm restart (SDGR) [23]. Our T_i was chosen to be 20 to be initial period, after which every time it is reached, the period is doubled.

5.2 Area Model

The area model constitutes a comparatively simpler inference problem and therefore admits a substantially reduced network architecture. The critical scale for this task is the signal area corresponding to the TE polarization of the proton, which represents the smallest physically relevant signal amplitude encountered in practice. Achieving low relative error at this scale ensures quality calibration and robust performance across all higher-polarization regimes, where signal amplitudes are correspondingly larger.

We therefore use the area model as a controlled test case to examine how generalization performance evolves with model complexity in a relatively low-dimensional NMR problem. Based on this study, we find that a basic MLP architecture consisting of two hidden layers with 20 neurons each is sufficient to meet the accuracy and precision requirements of this task.

5.3 Denoising Autoencoder

In parallel, we worked on developing a denoising autoencoder (DAE) [25, 35] designed to filter noisy signals and reconstruct the underlying lineshape. The autoencoder consists of an encoder function $f_\theta(\cdot)$ that maps an input signal $x \in \mathbb{R}^N$ into a compressed latent

representation $z \in \mathbb{R}^d$, and a decoder $g_\phi(\cdot)$ that reconstructs a clean estimate \hat{x} :

$$z = f_\theta(x), \quad \hat{x} = g_\phi(z). \quad (50)$$

A schematic diagram of a simplified denoising autoencoder (DAE) architecture is shown in Fig. 9. This diagram is intended solely as a conceptual representation; the full network used in this work comprises significantly higher-dimensional layers and cannot be depicted compactly without loss of clarity.

The input to the DAE consists of a frequency-domain NMR spectrum with a feature dimension of 500, corresponding to the number of frequency bins. The output layer is constructed with the same dimensionality to enable direct reconstruction of the denoised spectrum. The hidden layers implement a symmetric encoder–decoder structure, in which the feature dimensionality is progressively reduced from 500 down to a low-dimensional latent representation of size 4 and subsequently expanded back to 500. This compression and reconstruction are performed through a sequence of reductions and expansions by factors of two, resulting in a total of 12 hidden layers. Rectified linear unit (ReLU) activations are used between all intermediate layers to introduce nonlinearity, while a linear activation function is applied at the output layer to preserve the continuous-valued nature of the reconstructed signal.

To train the network in a denoising configuration, noise $\varepsilon \sim \mathcal{D}_\varepsilon$ is added to the clean signal to form a corrupted input $\tilde{x} = x + \varepsilon$. The DAE is optimized to minimize reconstruction error between $\hat{x} = g_\phi(f_\theta(\tilde{x}))$ and the clean target x using a mean-squared error (MSE) loss:

$$\mathcal{L}_{\text{DAE}}(\theta, \phi) = \frac{1}{N} \sum_{i=1}^N \|x_i - g_\phi(f_\theta(\tilde{x}_i))\|_2^2. \quad (51)$$

To preserve physically meaningful spectral structure (such as smooth curvature and peak shape), we include a second-derivative regularization penalty:

$$\mathcal{L}_{\text{smooth}} = \|\nabla^2 g_\phi(f_\theta(\tilde{x}))\|_2^2. \quad (52)$$

The total loss is therefore:

$$\mathcal{L} = \mathcal{L}_{\text{DAE}} + \lambda \mathcal{L}_{\text{smooth}}, \quad (53)$$

where λ controls the trade-off between target fidelity and smoothness. The trained autoencoder then acts as a noise-removal mapping,

$$\hat{x} = \mathcal{F}_{\theta, \phi}(x + \varepsilon). \quad (54)$$

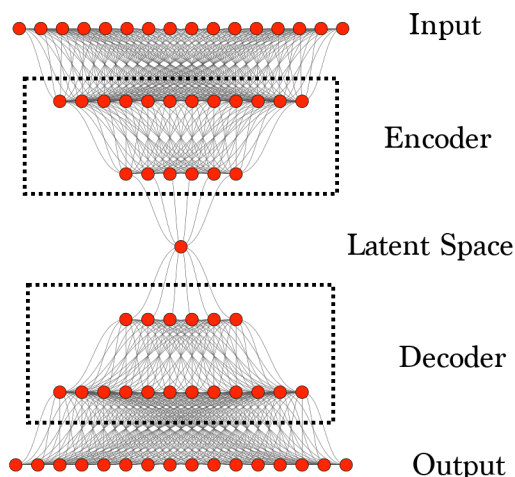


Fig. 9: Example diagram of a denoising autoencoder architecture (not to scale). Diagram made with NN-SVG [21].

5.4 Training

Training was performed using datasets generated through MC simulations. For each simulated event, a baseline parameterization is randomly sampled according to the formalism described in Sec. 2, after which the NMR signal is constructed using the appropriate lineshape model. Gaussian-distributed noise is then added independently to each of the 500 frequency bins to emulate stochastic electronic and RF noise. The resulting composite spectrum is stored as a simulated polarized-target NMR event, representing a realistic approximation of an experimentally recorded NMR spectrum obtained from the accumulation of multiple NMR sweeps.

For the polarization models, simulated signals were generated using polarization values drawn uniformly from the ranges 2–60% for the high-polarization model (a CNN with 373k trainable parameters) and 0–2% for the low-polarization model (a CNN with 234k trainable parameters). For the low-polarization simulations, a gain factor of 50 was applied to the synthesized lineshapes, corresponding to the maximum gain available on the Liverpool Q-meter. This scaling ensures that the simulated signal amplitudes and noise levels are representative of those achievable under realistic experimental conditions.

For the area model, simulated signals were generated over the full polarization range of 100%. Polarization values near the proton thermal-equilibrium (TE) region, up to 1%, were intentionally oversampled using a uniform distribution, while values above 1% were sampled according to an inverse-exponential distribution. This sampling strategy increases the statistical weight of

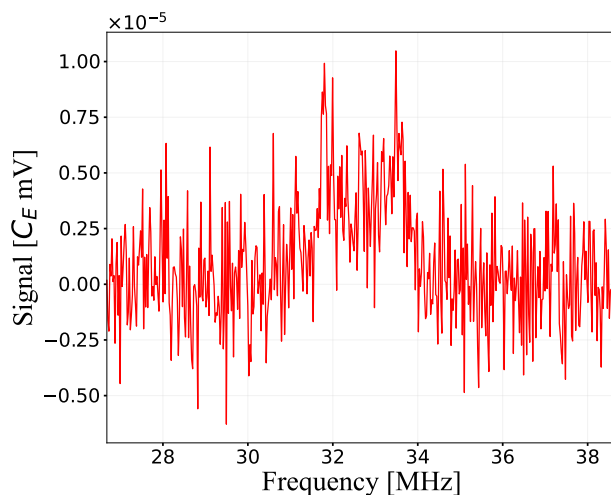


Fig. 10: Simulation of TE signal with “high level” of noise injected with SNR = 1.11. (double the normal scale shown in Fig. 2).

low-polarization events, which would otherwise be underrepresented in a purely uniform dataset, and ensures that the model learns to resolve the smallest physically relevant signal areas with high fidelity.

By emphasizing this low-area regime during training, the model is forced to develop sensitivity to subtle variations in signal area that dominate the error budget near TE, while naturally retaining strong performance at higher polarization values where the signal-to-noise ratio and feature contrast are larger.

For the DAE, training data were generated over a polarization range of 0–60%, with the region near the TE polarization up to 1% intentionally oversampled to emphasize the most noise-sensitive regime. Because the DAE is tasked with learning an implicit representation of the underlying physical lineshape through reconstruction, stochastic noise was injected only during training to corrupt the input spectra. This approach forces the encoder to learn a compact latent representation that captures the invariant spectral structure while discarding noise-dependent fluctuations.

Validation and test samples were intentionally kept noiseless. This choice ensures that loss evaluation probes the fidelity with which the latent space encodes the intrinsic NMR lineshape, rather than rewarding overfitting to specific noise realizations. By decoupling noise injection from validation and testing, the training procedure preserves the embedded physical constraints of the reconstruction task and yields a latent representation that generalizes robustly across noise conditions encountered during inference.

Training, validation, and testing datasets were split according to an 80/10/10 ratio. All models were initially trained for 1000 epochs with a batch size of 256. If the validation loss continued to decrease, the model weights were reloaded and training was resumed until overfitting began to appear. Model training was performed using the PyTorch API [26], with the AdamW [22] optimizer, chosen for its robust performance in a wide range of applications. In general, each model should be trained on a dataset containing at least an order of magnitude more independent training samples than the number of free trainable parameters, with the precise requirement depending on the effective model complexity. For the initial benchmarking studies presented here, each model was trained using one million simulated data events, corresponding to deuteron NMR signals superimposed on realistic Q-meter baselines and spanning a broad range of polarization values and noise conditions. Hyperparameters were optimized using Optuna [3], a Bayesian optimization framework that performs iterative trials to identify optimal hyperparameter configurations within predefined constraints. We ran 200 trials per model to determine near-optimal configurations, save for the low-polarization model, for which we used the same optimized hyperparameters as the high-polarization model. These tuned hyperparameters are shown in Tables 1 and 2. During training, noise was injected on a 2.6 SNR scale, (low noise). This scale is shown in the bottom plot of Fig. 2. Additional, 1.3 SNR (high noise) is also used for more extreme validation (see Fig. 10). This noise was sampled from a normal distribution $\mathcal{N}(0, \sigma)$, where the mean is zero and σ is the standard deviation of the noise. From experimental signals, this was found to be on the order of 10^{-6} mV. Discussions in this paper of “high noise” regions corresponds to noise sampled from a normal distributed with double this standard deviation.

Model training is ideally performed either in a single uninterrupted session or through the use of checkpointing, such that the optimized model state and optimizer parameters are preserved and training can resume seamlessly from the point of interruption. This approach is particularly important for models that require extended training times or are trained on large datasets.

Figure 11 shows a representative training history for the area model. The spike marked by the green vertical dotted line corresponds to a point at which the model weights were reloaded without restoring the associated optimizer state; as a consequence, the optimizer was effectively reinitialized, producing a transient increase in the loss. The red star denotes the epoch at which the minimum validation loss was achieved, corresponding to the optimal set of model weights and biases, which were subsequently saved as the final trained model. For all CNN

models, a total of one million simulated events were generated for the complete training procedure, with the dataset partitioned according to an 80/10/10 split into training, validation, and testing subsets.

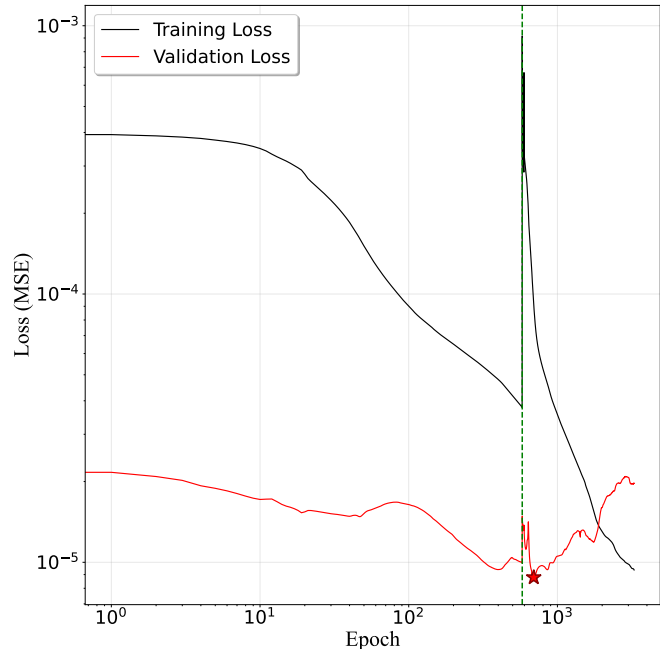


Fig. 11: Loss/Validation Loss vs. Epoch for area model (log-log scaling). Early stopping was applied when the model started to overfit (i.e., after 500 epochs without any improvement). The red star indicates the lowest validation loss achieved; the model weights and biases as this point were used as the final model.

6 Results

In this section, we present the evaluation of the four specialized model classes introduced above. Their performance is assessed using independently generated test data that systematically vary in polarization, lineshape, baseline drift, and SNR. This allows us to characterize the strengths and limitations of each model architecture—MLP, CNN, DAE and the hybrid variants—in terms of accuracy, precision, stability under distribution shifts, and sensitivity to both statistical and systematic variations in the underlying NMR signals.

Both the polarization and area models were evaluated using simulated NMR spectra generated with the simulated baseline and signal lineshape formalism described in Secs. 2 and 3.1 respectively. For each simulated target event we passed the resulting spectrum to the model to obtain inferred values of polarization, area or

NMR signal in the case of the DAE. This procedure was repeated many times (typically 1000 trials) across the full polarization range (or specialized range) to quantify both the mean and spread of the distribution of the residuals.

6.1 Standard Fits

An error evaluation of the standard, non-AI-based, lineshape fitting procedure for Pake-doublet signals was performed using the same simulated data sets employed to benchmark the AI models. The analysis consists of baseline subtraction, followed by a third-order polynomial χ^2 fit to the spectral wings, which is subsequently subtracted leaving only the target signal. A Dulya fit [9] is then applied to extract the polarization. The quality of this fit is strongly polarization dependent, with higher polarization values yielding substantially better fits. To enable a direct comparison with our AI-based models, this study was carried out over the same polarization ranges. For polarization values between 10–60%, the average relative error is approximately 3.5% over the same 1000 trials as used in the AI approach. Below 10% polarization, the error increases rapidly for smaller signals especially with reduced signal-to-noise. In the TE regime the relative error can approach 100% when noise is large or fitting is poor. For the best cases with nominal noise level and well centered signals, the lowest relative errors obtained were in the range of 5-7% relative. But this was only true for about 10% of the generated data.

A comparable evaluation was performed for the area-based method using proton-like signals. In this case, the procedure similarly involves baseline subtraction, a third-order polynomial χ^2 fit to the spectral wings with subsequent subtraction, followed by numerical integration of the signal using a Riemann-sum approach [16] to extract the area. At the TE polarization scale (0.3% polarized), the resulting average relative error is approximately 2.5%.

6.2 Polarization Models

Across the high-polarization regime (2–60%), the best-performing feedforward MLP achieved a residual mean of 0.107% with a residual spread of 0.992%, corresponding to an effective polarization error of approximately 1.2% relative. In contrast, the fully optimized CNN architecture attained a residual mean of -0.058% with a residual spread of 0.105%, leading to a relative polarization error of roughly 0.15%. The residual distribution for the high-polarization model, evaluated throughout the polarization range (2–60%) using Gaussian

noise that spans SNR values of 2 to 10, is shown in Fig. 12.

The CNN-based model developed for the low-polarization regime (0–2%) significantly outperforms the corresponding MLP-based architecture. When evaluated on noiseless test data, the CNN yields a mean residual of $3 \times 10^{-5}\%$ with a residual standard deviation of $2.3 \times 10^{-4}\%$, demonstrating excellent intrinsic accuracy and precision for such a small scaled signal.

Under realistic noise conditions with signal-to-noise ratios in the range $\text{SNR} \approx 5\text{--}10$, the model maintains strong performance, achieving a mean residual of $7.00 \times 10^{-4}\%$ and a residual spread of $3.03 \times 10^{-3}\%$. Even in more challenging conditions, with noise sampled over $\text{SNR} \approx 1\text{--}5$, the CNN-based model continues to perform robustly, with a mean residual of $-2.31 \times 10^{-3}\%$ and a precision of $5.08 \times 10^{-3}\%$.

When translated to the TE polarization scale relevant for the spin-1 Pake doublet, these residuals correspond to an average relative uncertainty of approximately 3.4%. Table 3 summarizes the overall accuracy and precision achieved by both the MLP- and CNN-based models in the high- and low-polarization regimes. As evidenced in the table, the CNN-based architecture consistently outperforms the MLP-based model across both polarization ranges.

Model	Accuracy	Precision
High-P CNN	99.57%	0.105%
Low-P CNN	99.42%	0.003%
High-P MLP	95.61%	0.992%
Low-P MLP	92.45%	0.012%

Table 3: Accuracy and precision metrics for the polarization models.

Because the training data are uniformly distributed in polarization, model accuracy and precision naturally vary across different test regions. This behavior primarily reflects changes in the NMR lineshape as a function of polarization: depending on the local structure of the lineshape, a model may exhibit a trade-off between bias (accuracy) and variance (precision) in specific polarization intervals, while maintaining roughly constant overall performance (see Table 4). An example is shown in Fig. 13, which displays residuals from 1000 inference trials at a fixed true polarization of 5% under varying noise and baseline conditions. Two representative noise regimes are shown: a low-noise case ($\text{SNR} = 2.6$) and a higher-noise case ($\text{SNR} = 1.3$). The corresponding mean and standard deviation of the inferred values are summarized in Table 5. For the high-polarization model, the difference between these two noise conditions is

minimal, and even at the lowest tested polarization the overall signal strength remains large compared to the injected noise.

Range	Low Noise Res.		High Noise Res.	
	Mean (%)	Std (%)	Mean (%)	Std (%)
10–15%	0.244918	0.055281	0.245454	0.058145
20–25%	0.086172	0.195207	0.097808	0.193600
30–35%	0.094028	0.251061	0.068316	0.257707
40–45%	0.150626	0.211104	0.147776	0.215561
50–55%	0.349871	0.069383	0.348094	0.073787

Table 4: Results of testing the 2-60% model for low noise (13-476 signal-to-noise) and high noise (6-180 signal-to-noise) ranges.

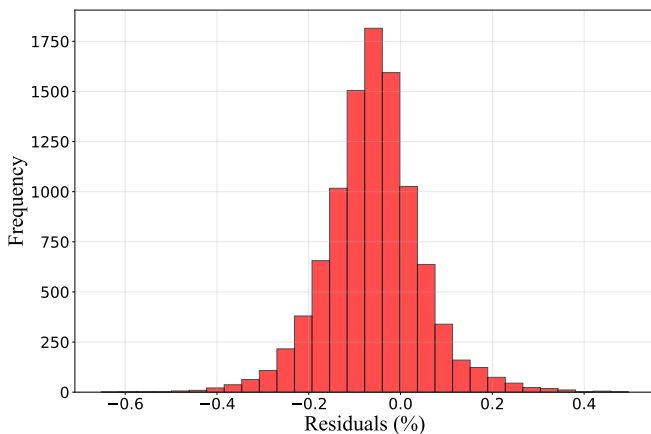


Fig. 12: Distribution of polarization residuals for the range of 2-60%. SNR values ranged from ~ 5 -300. The mean residual is -0.058% and the width is 0.105% .

6.3 Area Model

We first examined the area-extraction problem under idealized conditions in order to establish a benchmark for achievable performance. In the absence of frequency-dependent distortions—specifically when the proton NMR peak position is fixed and the Q-meter baseline exhibits neither tune shifts nor discontinuous jumps—the relationship between integrated signal area and polarization is approximately linear over the full dynamic range. Under these conditions, a simple linear ridge regression model is sufficient to achieve a relative error of approximately 0.63% in the TE region for the proton.

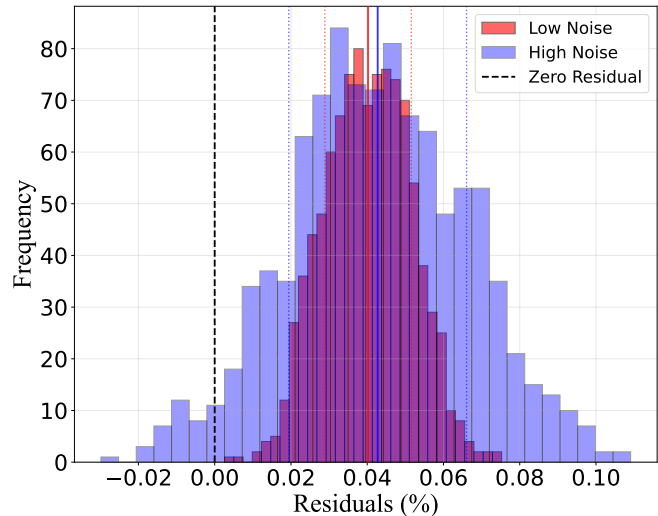


Fig. 13: Distribution of residuals for polarization of $P = 5\%$ from 1000 inference tests with the high-polarization model. **Red**: The Gaussian noise applied gives an SNR around 30. **Blue**: The same Gaussian noise (doubled), giving an SNR of 15. Statistics for mean and standard deviation are shown in Table 5.

Here, the ridge model refers to a linear regression augmented with an ℓ_2 regularization term on the model coefficients. This regularization suppresses sensitivity to noise and mitigates overfitting when training data are limited, while preserving the underlying linear mapping between signal area and polarization. Owing to the near-linearity of the area-polarization relationship, this approach remains effective even when trained on a relatively small dataset of $\sim 5 \times 10^3$ events under nominal noise conditions.

When extending the training to more realistic experimental scenarios—including variations in the NMR peak position, baseline tune shifts, and small discontinuities in the Q-curve—the effective mapping between signal area and polarization becomes nonlinear. In this regime, a purely linear model is no longer sufficient, and sub-percent relative error at the TE scale cannot be maintained. Introducing modest nonlinearity by augmenting the model with two hidden layers of 20 neurons each restores performance, allowing the model to again achieve relative errors below 0.7% in the TE region, provided that the training dataset is increased to at least $\sim 5 \times 10^4$ events.

For completeness, we also evaluated a CNN architecture—identical in form to that used for the polarization models—on the area-extraction task. While the CNN is capable of achieving comparable relative error, doing so requires substantially larger training datasets, on the order of 10^6 events. This reflects the greater model

capacity and weaker inductive bias of the CNN for a problem that is fundamentally low dimensional and dominated by global amplitude information rather than localized spectral features.

Figure 14 shows the distribution of residuals between the predicted and true signal area for the CNN-based area model across the full tested polarization range for a proton like signal. For 1000 independent inference trials, the mean residual of $2.9855 \times 10^{-8} \text{ mV} \cdot \text{MHz}$ corresponds to an accuracy of 99.787%, with a residual width of $1.288 \times 10^{-5} \text{ mV} \cdot \text{MHz}$.

The area model successfully generalized to any realistic lineshape inferring only the total area under the curve. Fig. 15 shows the results for a deuteron type Pake doublet lineshape area test. The figure presents overlapping histograms of the residual distributions obtained under low-noise (SNR = 2–10) and high-noise (SNR = 1–5) conditions. These distributions were generated by repeatedly injecting independent noise realizations into a fixed underlying signal over 1000 trials, enabling a systematic characterization of noise-induced error. The corresponding mean and standard deviation values are summarized in Table 5. Even in the high-noise regime, the resulting residuals correspond to a relative error of approximately 0.6%, demonstrating the robustness of the trained model.

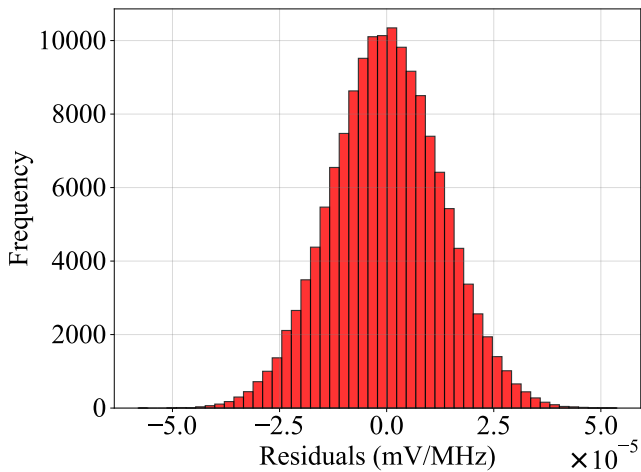


Fig. 14: Distribution of residuals in area model for the polarization range of TE to 60%. The SNR range for this test 6-77.

6.4 Denoising Autoencoder Model

The denoising autoencoder (DAE) model is designed to suppress stochastic noise while preserving the underlying

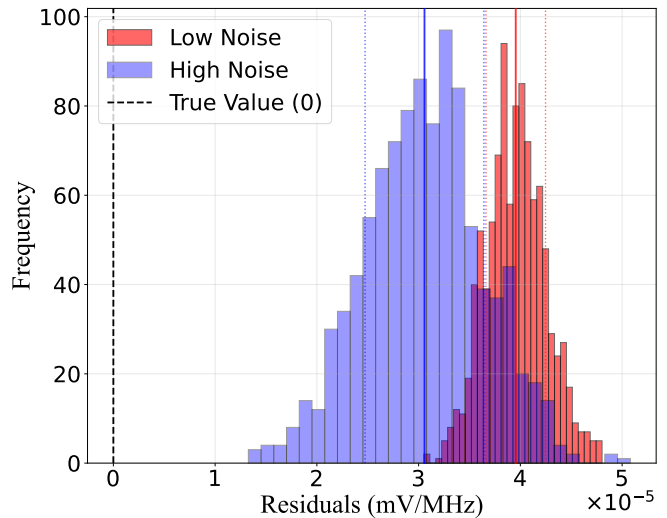


Fig. 15: Distribution of residuals from the area model for a polarization of $P = 5\%$ over 1000 trials of inference for the polarization range of TE to 60% for a separate preliminary ND3 area model. The SNR range for this test for low (red) was ~ 30 and for high (blue) was ~ 15 . The mean and standard deviation are shown in Table 5.

Table 5: Residual statistics for polarization (P) and area (A) from sampling for an event at $P = 5\%$.

	Noise	μ	σ
$P(\%)$	Low	0.040	0.011
	High	0.043	0.023
$A(\text{mV/MHz})$	Low	4×10^{-5}	3×10^{-6}
	High	3×10^{-5}	6×10^{-6}

NMR signal structure. In this architecture, the input to the model consists of a noisy frequency-domain spectrum comprising 500 frequency bins, and the output is a spectrum of identical dimensionality in which the noise component is substantially reduced.

Figs. 16 and 17 show representative examples of the DAE’s performance. Fig. 16 shows the denoising applied to a simulated NMR lineshape with a signal-to-noise ratio of approximately unity, corresponding to a polarization level of 5%. Fig. 17 presents an example using real experimental data acquired under typical noise conditions. In addition, Fig. 18 demonstrates the DAE’s performance on experimental data collected with the NMR coil positioned approximately 10 mm away from the target cup to permit mechanical rotation, a configuration that introduces elevated noise and reduced coupling.

6.5 Comparison

For the high-polarization model, we observe an improvement in the fit error exceeding an order of

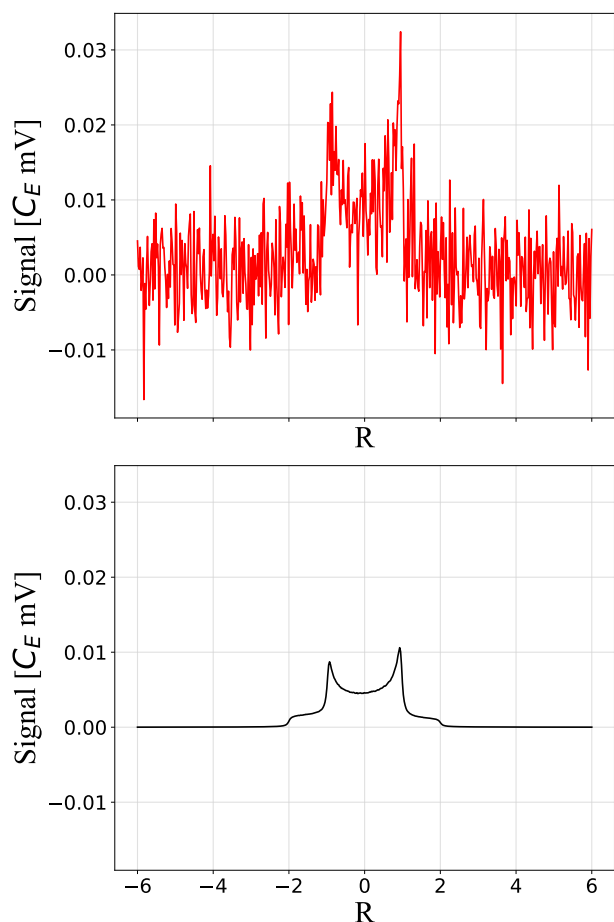


Fig. 16: Example usage of DAE on simulated lineshape event. **Top:** Input signal with large amount of noise. **Bottom:** Reconstructed signal. SNR for this example is 0.8045.

magnitude relative to standard, non-AI-based extraction methods. In the low-polarization regime, the resulting error remains larger when using nominal SNR achieving 3.4% relative for the TE range which is still better than what is possible by traditional means at the TE scale for spin-1 which is around 5% relative at in the best circumstances. For the area-based model, we again observe a substantial reduction in relative error, again approaching an order of magnitude improvement compared to traditional methods. This direct, one-to-one comparison with standard non-AI approaches clearly demonstrates the performance gains afforded by the proposed AI-based techniques. Additionally, as pointed out earlier, we are using limited training data for each of the model types to reduce training time. For real-world deployment substantially more training would result in improved results and lower overall error.

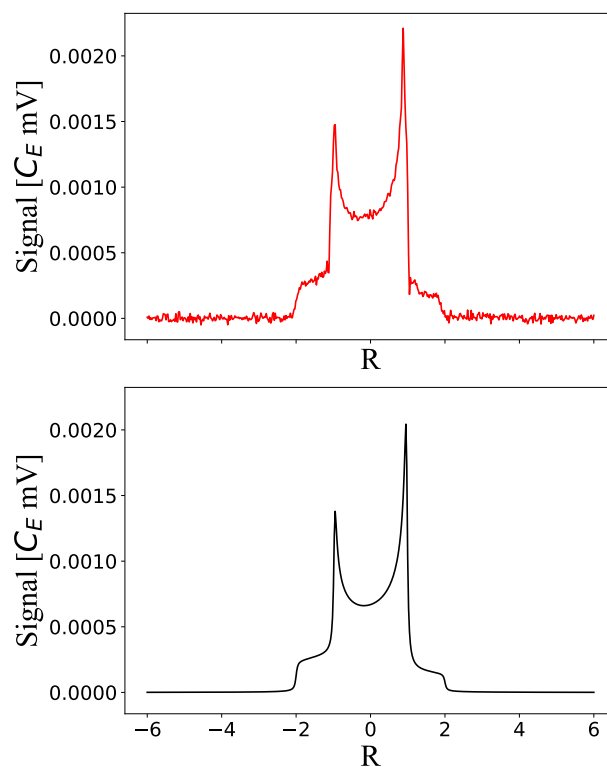


Fig. 17: Example of DAE being used on a real experimental signal under typical lab conditions with typical noise level for a single sweep NMR. Polarization of the real signal for irradiate d-butanol is approximately 44%.

Although these models achieve substantial reductions in fitting-related uncertainty, it is important to acknowledge instrumental limitations that the AI-based methods considered here cannot directly circumvent. In particular, reducing the extraction error to levels well below the Q-meter's intrinsic relative accuracy of approximately 1% does not translate into a proportional improvement in the overall measurement precision. While such reductions effectively render the fitting uncertainty negligible within the total error budget, a Q-meter-based NMR system cannot exceed this fundamental performance limit without corresponding advances in hardware design and instrumentation.

In addition, the achievable lower bound on the overall polarization uncertainty is constrained by several experimental factors. These include the coupling between the NMR coil and the target material, the spatial distribution of the beam across the sample—leading to nonuniform radiation damage—the distribution of microwave power throughout the target, and distortions in the magnetic-field homogeneity over the sample volume. Most notably, the inherently limited TE measurements during experiments, particularly for proton targets when

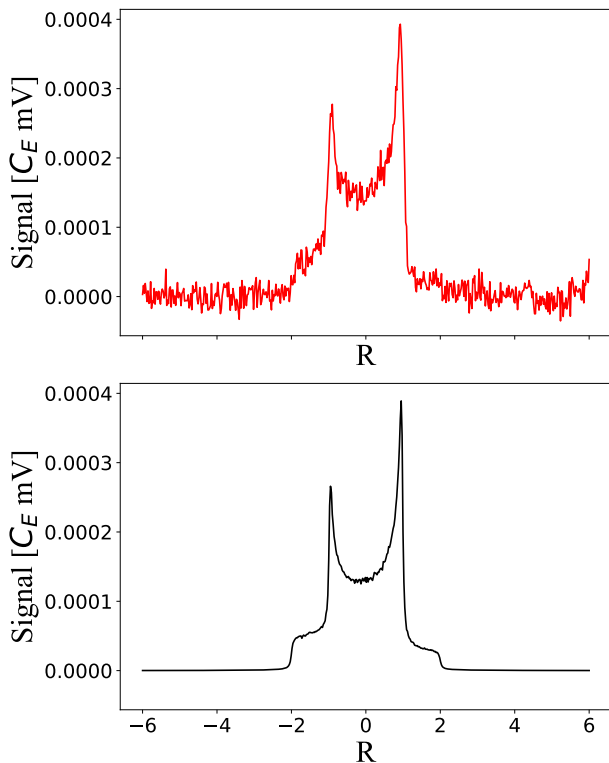


Fig. 18: Another example of DAE being used on a real experimental with the coil outside the target material making a significantly worse SNR. The signal shown here was acquired using an irradiated d-butanol sample with an estimated polarization of approximately 45%.

relying on the area-based method, places a stringent bound on the extent to which offline analysis can further reduce the total uncertainty.

From the perspective of online monitoring and real-time feedback, inference speed constitutes an additional point of comparison between traditional and AI-based analysis methods. Conventional approaches—consisting of background subtraction, polynomial fitting and subtraction of the spectral wings, followed by numerical integration of the remaining signal—can typically be executed on time scales of a few hundred milliseconds per spectrum. This performance is generally adequate when many NMR sweeps are accumulated and averaged over time scales of seconds or more. However, such latencies are suboptimal for applications requiring rapid signal processing, adaptive response, or real-time system control.

By contrast, all AI-based models considered here produce inference outputs on millisecond time scales on CPU systems, with further speed gains achievable through model optimization and hardware acceleration. This capability enables near-real-time analysis of individual or

minimally averaged spectra. Moreover, for more sophisticated analyses—such as Dulya-type fits used to extract vector and tensor polarizations—no comparably fast traditional implementation currently exists, as these procedures are computationally intensive and often require manual intervention to ensure stable convergence. In this regard, AI-based inference offers a clear advantage in both speed and operational autonomy.

7 Tensor Enhanced Measurements

Beyond vector polarization extraction, these same tools facilitate real-time tensor polarization extraction at errors that are on the same scale as those obtained with the AI-based extraction for vector polarization. This improvement is a result of the direct extraction from the lineshape training, completely independent of the vector polarization value eliminating the need to propagate the vector polarization error to the tensor polarization.

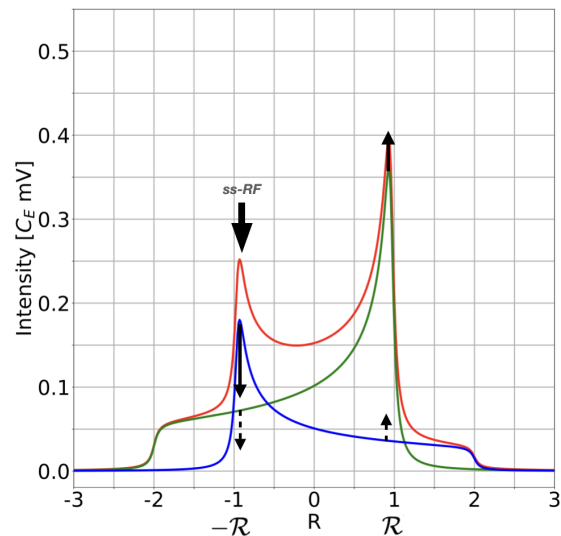


Fig. 19: Application of ss-RF at the resonance position $-\mathcal{R}$ of the Deuterium lineshape to reduce vector polarization [5].

Incorporating ss-RF signal manipulations [5] directly into the simulation and training pipeline to obtain reliable extraction of the enhanced tensor polarization, as shown in Fig. 19, is the next natural step. To support this, we will investigate the use of differential binning to train the network to predict individual absorption components, enabling simultaneous extraction of both vector and tensor polarization of an RF manipulated signal at millisecond timescales under various noise conditions. We also plan to

explore physics-informed architectural constraints [28], including domain-aware regularization [30] and symmetry priors [4]. When combined with simulated ss-RF perturbations over various frequency segments, we anticipate achieving a model capable of extracting high-fidelity polarization measurements under manipulations where conventional analysis methods fail. This new analysis will be presented in future work.

8 Conclusion

In this work, we have demonstrated that deep neural network-based approaches provide a robust and practical extension to conventional CW-NMR polarimetry for dynamically polarized targets. By training on physically realistic simulations that incorporate baseline distortions, tune shifts, and multiple noise sources characteristic of Q-meter-based systems, these models substantially reduce fitting-related uncertainties that have historically limited the precision and stability of polarization extraction. The resulting improvements translate directly into enhanced robustness for both real-time (online) monitoring and high-precision offline analysis, yielding a measurable increase in the experimental figure of merit.

Across a broad polarization range, the proposed AI-based polarization and area models outperform traditional TE- and lineshape-based methods under realistic noise and baseline conditions, particularly in regimes where conventional fitting becomes unstable or biased. In parallel, the denoising autoencoder provides an effective mechanism for suppressing stochastic noise while preserving physically meaningful spectral structure, enabling downstream extraction methods to operate on cleaner, more interpretable signals. Together, these components form a flexible analysis framework that decouples noise suppression, signal interpretation, and polarization inference in a manner not achievable with traditional pipelines.

At the same time, it is important to emphasize that these methods do not circumvent fundamental instrumental constraints. While neural networks can reduce extraction and fitting uncertainties well below the percent level, the ultimate lower bound on achievable polarization precision remains set by intrinsic limitations of the Q-meter system, thermal-equilibrium calibration accuracy, coil-sample coupling, field homogeneity, and target-specific experimental conditions. In this sense, the principal impact of the AI-based approach is the elimination of avoidable analysis-induced error, thereby allowing the total uncertainty to be dominated by well-understood physical and instrumental effects.

From an operational standpoint, the millisecond-scale inference times achieved by all models represent a

significant advantage for online monitoring and adaptive system control. Unlike traditional Dulya-type or area-based fits—which are computationally intensive and often require manual intervention—AI-based inference enables autonomous, high-rate polarization estimation suitable for feedback-driven optimization during data taking. This capability is particularly relevant for experiments operating under rapidly changing conditions or constrained beam-time schedules.

Looking forward, several avenues exist for further refinement. Improving performance in the extreme low-polarization and high-noise regimes will require targeted architectural optimization and expanded training datasets. In particular, neuron-pruning and model-compression strategies offer a promising route to reducing model complexity while simultaneously improving inference speed and generalization. In parallel, continued development of the denoising autoencoder—especially its integration with polarization and area models—will further strengthen the global analysis pipeline.

Finally, the methodology presented here is not limited to a single target material or spin species. Extending the area-based framework to encompass both spin- $\frac{1}{2}$ and spin-1 systems within a unified model will enhance adaptability during experimental target changes and facilitate broader deployment across polarized-target programs. Taken together, these results establish deep-learning-assisted CW-NMR polarimetry as a viable, high-performance tool for next-generation polarized scattering experiments.

9 Acknowledgments

The authors acknowledge Research Computing at the University of Virginia for providing computational resources and technical support that have contributed to the results reported in this publication. For additional information, see <https://rc.virginia.edu>. This work was supported by the U.S. Department of Energy under contract DE-FG02-96ER40950.

References

- [1] A. Abragam and L. C. Hebel. “The Principles of Nuclear Magnetism”. In: *American Journal of Physics* 29 (12 1961). ISSN: 0002-9505. DOI: 10.1119/1.1937646.
- [2] Anatole Abragam. *The principles of nuclear magnetism*. Repr. The international series of monographs on physics. Oxford: Clarendon Pr, 1986. 599 pp. ISBN: 9780198512363.

- [3] Takuya Akiba et al. *Optuna: A Next-generation Hyperparameter Optimization Framework*. 2019. arXiv: 1907.10902 [cs.LG]. URL: <https://arxiv.org/abs/1907.10902>.
- [4] Michael M. Bronstein et al. *Geometric Deep Learning: Grids, Groups, Graphs, Geodesics, and Gauges*. 2021. arXiv: 2104.13478 [cs.LG]. URL: <https://arxiv.org/abs/2104.13478>.
- [5] Joseph Clement and Dustin Keller. “Manipulation of spin-1 solid-state targets”. In: *Nuclear Instruments and Methods in Physics Research Section A: Accelerators, Spectrometers, Detectors and Associated Equipment* 1050 (2023), p. 168177. ISSN: 0168-9002. DOI: <https://doi.org/10.1016/j.nima.2023.168177>. URL: <https://www.sciencedirect.com/science/article/pii/S0168900223001675>.
- [6] G R Court et al. “A high precision Q-meter for the measurement of proton polarization in polarised targets”. In: *Nuclear Instruments and Methods in Physics Research Section A: Accelerators, Spectrometers, Detectors and Associated Equipment* 324 (3 1993), pp. 433–440. ISSN: 0168-9002. DOI: [https://doi.org/10.1016/0168-9002\(93\)91047-Q](https://doi.org/10.1016/0168-9002(93)91047-Q). URL: <https://www.sciencedirect.com/science/article/pii/016890029391047Q>.
- [7] G.R. Court and M.A. Houlden. “Modeling Non-Constant Current Effects for a Series Tune NMR Q-Meter Used for Nucleon Polarization Measurements”. In: *Proceedings of the Workshop on NMR in Polarized Targets*. University of Virginia, Charlottesville, VA, U.S.A., 1998, pp. 35–45.
- [8] D. G. Crabb and W. Meyer. “Solid polarized targets for nuclear and particle physics experiments”. In: *Annual Review of Nuclear and Particle Science* 47 (1997), pp. 67–109. DOI: 10.1146/annurev.nucl.47.1.67.
- [9] C. Dulya et al. “A line-shape analysis for spin-1 NMR signals”. In: *Nuclear Instruments and Methods in Physics Research, Section A: Accelerators, Spectrometers, Detectors and Associated Equipment* 398 (2-3 1997). ISSN: 01689002. DOI: 10.1016/S0168-9002(97)00317-3.
- [10] Ian Goodfellow, Yoshua Bengio, and Aaron Courville. *Deep Learning*. Book in preparation for MIT Press. MIT Press, 2016. URL: <http://www.deeplearningbook.org>.
- [11] Trevor Hastie, Robert Tibshirani, and Jerome Friedman. *The Elements of Statistical Learning*. Springer Series in Statistics. New York, NY, USA: Springer New York Inc., 2001.
- [12] Kaiming He et al. *Deep Residual Learning for Image Recognition*. 2015. arXiv: 1512.03385 [cs.CV]. URL: <https://arxiv.org/abs/1512.03385>.
- [13] Kurt Hornik, Maxwell Stinchcombe, and Halbert White. “Multilayer feedforward networks are universal approximators”. In: *Neural Networks* 2.5 (1989), pp. 359–366. ISSN: 0893-6080. DOI: [https://doi.org/10.1016/0893-6080\(89\)90020-8](https://doi.org/10.1016/0893-6080(89)90020-8). URL: <https://www.sciencedirect.com/science/article/pii/0893608089900208>.
- [14] Jie Hu et al. *Squeeze-and-Excitation Networks*. 2019. arXiv: 1709.01507 [cs.CV]. URL: <https://arxiv.org/abs/1709.01507>.
- [15] D. Keller. “Modeling alignment enhancement for solid polarized targets”. In: *European Physical Journal A* 53 (7 2017). ISSN: 1434601X. DOI: 10.1140/epja/i2017-12344-0.
- [16] D. Keller. “Uncertainty minimization in NMR measurements of dynamic nuclear polarization of a proton target for nuclear physics experiments”. In: *Nuclear Instruments and Methods in Physics Research Section A: Accelerators, Spectrometers, Detectors and Associated Equipment* 728 (2013), pp. 133–144. ISSN: 0168-9002. DOI: <https://doi.org/10.1016/j.nima.2013.06.103>. URL: <https://www.sciencedirect.com/science/article/pii/S0168900213009625>.
- [17] D. Keller, D. Crabb, and D. Day. “Enhanced tensor polarization in solid-state targets”. In: *Nuclear Instruments and Methods in Physics Research, Section A: Accelerators, Spectrometers, Detectors and Associated Equipment* 981 (2020). ISSN: 01689002. DOI: 10.1016/j.nima.2020.164504.
- [18] William Frederick Kielhorn. “A technique for Measurement of Vector and Tensor Polarization in Solid Spin One Polarized Targets”. In: *Proceedings of the 4th International Workshop on Polarized Target Materials and Techniques*. 1984.
- [19] Teerath Kumar et al. *Image Data Augmentation Approaches: A Comprehensive Survey and Future directions*. 2023. arXiv: 2301.02830 [cs.CV]. URL: <https://arxiv.org/abs/2301.02830>.
- [20] Yann LeCun, Koray Kavukcuoglu, and Clément Farabet. “Convolutional networks and applications in vision”. In: *Circuits and Systems (ISCAS), Proceedings of 2010 IEEE International Symposium on*. IEEE. 2010, pp. 253–256.
- [21] Alexander LeNail. “NN-SVG: Publication-Ready Neural Network Architecture Schematics”. In: *Journal of Open Source Software* 4.33 (2019),

- p. 747. DOI: 10.21105/joss.00747. URL: <https://doi.org/10.21105/joss.00747>.
- [22] Ilya Loshchilov and Frank Hutter. *Decoupled Weight Decay Regularization*. 2019. arXiv: 1711.05101 [cs.LG]. URL: <https://arxiv.org/abs/1711.05101>.
- [23] Ilya Loshchilov and Frank Hutter. *SGDR: Stochastic Gradient Descent with Warm Restarts*. 2017. arXiv: 1608.03983 [cs.LG]. URL: <https://arxiv.org/abs/1608.03983>.
- [24] W. Meyer and E. Schilling. “Tensor Polarized Deuteron Target for Intermediate Energy Physics”. In: *Proceedings of the 4th International workshop on Polarized Target Materials and Techniques*. 1984.
- [25] Umberto Michelucci. *An Introduction to Autoencoders*. 2022. arXiv: 2201.03898 [cs.LG]. URL: <https://arxiv.org/abs/2201.03898>.
- [26] Adam Paszke et al. *PyTorch: An Imperative Style, High-Performance Deep Learning Library*. 2019. arXiv: 1912.01703 [cs.LG]. URL: <https://arxiv.org/abs/1912.01703>.
- [27] S. I. Pentillä. “Workshop on NMR in Polarization Targets”. In: *Proceedings of the Workshop on NMR in Polarized Targets*. Charlottesville, VA: University of Virginia, 1998, pp. 15–26.
- [28] M. Raissi, P. Perdikaris, and G.E. Karniadakis. “Physics-informed neural networks: A deep learning framework for solving forward and inverse problems involving nonlinear partial differential equations”. In: *Journal of Computational Physics* 378 (2019), pp. 686–707. ISSN: 0021-9991. DOI: <https://doi.org/10.1016/j.jcp.2018.10.045>. URL: <https://www.sciencedirect.com/science/article/pii/S0021999118307125>.
- [29] Connor Shorten and Taghi M Khoshgoftaar. “A survey on image data augmentation for deep learning”. In: *Journal of Big Data* 6.1 (2019), pp. 1–48.
- [30] Skylar E. Stolte et al. *DOMINO++: Domain-aware Loss Regularization for Deep Learning Generalizability*. 2023. arXiv: 2308.10453 [cs.CV]. URL: <https://arxiv.org/abs/2308.10453>.
- [31] Christian Szegedy et al. *Going Deeper with Convolutions*. 2014. arXiv: 1409.4842 [cs.CV]. URL: <https://arxiv.org/abs/1409.4842>.
- [32] Vladimir N Vapnik. *Statistical Learning Theory*. New York: Wiley, 1998. ISBN: 978-0-471-03003-4.
- [33] Ashish Vaswani et al. *Attention Is All You Need*. 2023. arXiv: 1706.03762 [cs.CL]. URL: <https://arxiv.org/abs/1706.03762>.
- [34] Ragav Venkatesan and Baoxin Li. *Convolutional Neural Networks in Visual Computing: A Concise Guide*. English (US). Publisher Copyright: © 2018 by Taylor & Francis Group, LLC. All rights reserved. CRC Press, Oct. 2017. ISBN: 9781498770392. DOI: 10.4324/9781315154282.
- [35] Pascal Vincent et al. “Extracting and composing robust features with denoising autoencoders.” In: *ICML*. Ed. by William W. Cohen, Andrew McCallum, and Sam T. Roweis. Vol. 307. ACM International Conference Proceeding Series. ACM, 2008, pp. 1096–1103. ISBN: 978-1-60558-205-4. URL: <http://dblp.uni-trier.de/db/conf/icml/icml2008.html#VincentLBM08>.
- [36] Qingyun Zhang et al. “Data Augmentation for Deep Learning: A Survey”. In: *Journal of Big Data* 8.1 (2021), pp. 1–48. DOI: 10.1186/s40537-021-00499-4.